國立中山大學材料與光電科學學系

碩士論文

Department of Materials and Optoelectronic Science

National Sun Yat-sen University

Master Thesis

金屬玻璃鍍膜對鎂合金表面之硬度改質

Surface Hardness Improvement in Magnesium Alloy by Metallic-Glass Sputtered Film

研究生：陳柏佑

Bo-You Chen

指導教授：黃志青 博士

Dr. Jacob C. Huang

中華民國 100 年 7 月

July 2011

國立中山大學研究生學位論文審定書

本校材料與光電科學學系碩士班

研究生陳柏佑（學號：M983100008）所提論文

金屬玻璃鍍膜對鎂合金表面之硬度改質
Surface Hardness Improvement in Magnesium Alloy by Metallic-Glass Sputtered Film

經本委員會審查並舉行口試，符合碩士學位論文標準。

學位考試委員簽章：

謝克昌　　黃志青

高伯威

指導教授　黃志青

系主任/所長

Table of Content

List of Tables

List of Figures

致謝

即將結束兩年的碩士班生涯，回顧這些學習做研究的日子，從大學部的專題實驗到碩士論文。首先，我要感謝恩師　黃志青教授。老師除了在課業以及實驗的的指導，更花很多時間教導我們做人做事的道理。每當我們遇到困難，不論是研究上或是生活上的，老師總是會關心我們，並陪伴我們渡過低潮。除了研究，老師也很重視英文能力，幾年來利用英文的小測驗、競賽，甚至是英文的研究討論，來幫助我們增強英文能力。對於剛踏入研究領域懵懂無知的我來說，老師的訓練與照顧都是全方位的。

此外，在這充滿酸甜苦辣的兩年碩士生涯，非常感謝實驗室各位學長、學弟妹們的幫助以及支持，特別感謝剛進實驗室的時候，帶我入門的鴻昇學長；一起陪伴我做研究、學英文的良師益友—宇庭學長；可以陪我聊心事，以及指導我實驗的名哲學長、浩然、大豪學長；常常給予我們實驗啟發以及批判的敬仁、育誠、海明、炎暉等諸位學長。也謝謝從大學時代就一直陪伴我的好友昭憲，還有球隊裡常常帶給我歡笑的球伴們，讓我可以適時地調節生活緊湊的步調。

最後，我要感謝一路上無怨無悔為我付出的家人們，沒有他們默默的付出與支持，我就沒有辦法順利的完成我的學業。『天下沒有不散的筵席』。即使畢業之後，我都會常常想起這些良師益友們帶來的啟發，我會懷念這些年來在西子灣生活的點點滴滴，相信總有一天，我們一定會在社會上闖出自己的一片天，並且重逢分享這些喜悅。

摘要

鈀銅矽非晶質薄膜的玻璃形成能力和硬度佳,因此被選為用來改善 AZ31 鎂合金表面硬度的鍍層。實驗中，從三十到兩百奈米，不同厚度的鈀銅矽薄膜試片都會經過微硬度還有奈米壓痕的測試。硬度和相對應的壓印深度可由一種量化模型推算而出。相關的作用參數和硬度值可以經過反覆的計算得到。根據實驗結果顯示，鎂合金的淺層區表面硬度可以藉由鈀銅矽非晶質薄膜，隨著壓印深度的減少而大幅地提升。除此之外，使用比較薄的非晶質鍍層(例如兩百奈米)，基板和薄膜之間的作用會比較強。而使用比較厚的非晶質鍍層(例如兩千奈米)，較容易造成薄膜的破裂。本實驗估算，適當的非晶質薄膜厚度大約在兩百奈米左右。

關鍵字：鎂合金、硬度、濺鍍、非晶質薄膜、奈米壓痕

Abstract

The $Pd_{77}Cu_6Si_{17}$ (PCS) thin film metallic glasses (TFMGs) with high glass forming ability and hardness are selected as a hard coating for improving the surface hardness of the AZ31 magnesium alloy. Both micro- and nano-indentation tests are conducted on the specimens with various PCS film thicknesses from 30 to 2000 nm. The apparent hardness and the relative indentation depth (β) are integrated by a quantitative model. The involved interaction parameters and relative hardness values are extracted from iterative calculations. According to the results, surface hardness can be enhanced greatly by PCS TFMGs in the shallow region, followed by gradual decrease with increasing β ratio. In addition, the specimens with thinner coating (for example, 200 nm) show greater substrate-film interaction and those with thick coating (for example, 2000 nm) become prone to film cracking. The optimum TFMG coating thickness in this study is estimated to be around 200 nm.

Keywords: Magnesium alloys, hardness, sputtering, thin film metallic glass, nanoindentation

Chapter 1 Introduction

1-1 Characteristics of Mg alloys

Among many engineering materials, Mg alloys have raised much attention in recent years. For industrial need of developing high strength materials with light weight, Mg alloys have attracted more and more interests due to their specific strength among all structural materials. Because of the good recyclability, Mg alloys are regarded as a potential structural material.

The density of pure Mg (1.74 g/cm^3) is lower than that in pure Al (2.70 g/cm^3) and Ti (4.54 g/cm^3), but Mg shows a high strength to weight ratio among all structural materials. For thermal conductivity, compared with plastics, Mg alloys exhibit a high thermal conductivity due to good thermal dissipation. For damping and crash resistance, the damping resistance of Mg alloys is better than that of aluminum and plastics. The crash resistance of Mg alloys is notable to be superior to that of plastics. In electromagnetic shielding capability, the Mg wall can shield the electromagnetic wave effectively [1]. If electronic products are made of Mg alloys, or Mg alloys are coated on the surface of electronic products, the electromagnetic shielding capability may protect human bodies from electromagnetic wave damage.

Moreover, the good casting ability of Mg alloys makes it easier to be die-cast into complicated shapes. Similar to other alloys, Mg alloys can also be reused and recycled through remelting procedures. The recyclability makes Mg alloys possible to lower capital cost and economize the natural resources. This characteristic benefits the extension of commercial use of Mg alloys.

The above advantages make Mg alloys become irreplaceable in industry. For the computer, consumer and communication (3C) of electronic products, Mg alloys are used for the shell and radiator components. Moreover, Mg alloys show the good electromagnetic interference (EMI) capability. Mg alloys was regarded as a new family of promising materials in application of electronic products. Although Mg alloys exhibit a lot of advantages, there are still some undesirable properties: poor corrosion resistance, poor wear resistance, unsatisfactory creep resistance, and high chemical reactivity. Poor corrosion resistance drastically deteriorates the properties of Mg alloys in severe environments. High chemical reactivity will cause the formation of oxidization easily. In addition, Mg alloys have faced a challenging problem in the intrinsic properties, such as low hardness, and low strength. Compared with other industrial alloys, the strength of Mg alloys is too low to bear intense stress. These disadvantages restrict the engineering applications of Mg alloys. As a result, many efforts have been devoted to the improvement in these properties.

1-2 Classifications of magnesium alloys

For commercial Mg alloys, a variety of elements are added for the formation of solid solution, such as Al, Ce, Li, Ag, Th, Zn, and Zr [2]. In general, the main components and compositions of Mg alloys can be indicated by the capital letters and the followed numbers. Table 1-1 [3] presents the standard four-digit American Society for Testing and Material (ASTM) designation system for Mg alloys and their heat treatments in temper. The first two letters indicate two main components with abbreviations of the elements. A is the abbreviation of aluminum, C is for copper, E is for rare earths, F is for iron, H is for thorium, K is for zirconium, L is for lithium, Q is for silver, and Z is for zinc. The first letter describes the element which possesses a larger quantity than the other element in addition to Mg itself. If the quantities are equal of two components, the letters will be listed alphabetically. The numbers followed by the letters stand for the compositions of the above elements in weight percent (wt%). Taking AZ31B-H24 for example, it means that the alloy is composed of nominal 3 wt% aluminum, 1 wt% zinc, and is referred to B modification. B is used to distinguish the same AZ31 form that contains different levels of impurity. The H24 designation indicates that the alloy is strain-hardened and partially annealed.

The solute elements are usually added to Mg alloys for the improvement in casting capability, corrosion resistance, etc. For example, the addition of Al to Mg solvent is mainly for solute hardening and precipitation hardening through the $Mg_{17}Al_{12}$ β phase. The addition of Zn will enhance casting capability of the Mg alloys. The effects of various solutes on mechanical, corrosion, and casting behaviors are all listed in Table 1-2 [4]. Due to these advantages above, Mg alloys, such as AZ, AM, ZK series, have become popular in commercial markets.

1-3 Amorphous alloys

The structure of crystalline materials shows long-range-order (LRO) with repeating unit cell, as shown in Figure 1-1 [5]. Different from crystalline materials, the structure of amorphous alloys exhibits a disordered arrangement that lacks crystalline periodicity. The random atomic structures are displayed in amorphous alloys. Although amorphous alloys are considered to be random atomic arrangement, the atomic arrangements are not completely random but with a short-range-ordered (SRO) structure, as shown in Figure 1-2 [5]. Based on the structure and thermodynamic characteristics, amorphous alloys are called non-crystalline metals, liquid metals, glassy metals, or metallic glasses. Amorphous alloys show metal lustrous appearance and smooth surface, as shown in Figure 1-3 [6]. They are in contrast to the environmental transparent glasses.

To fabricate amorphous alloys in the form of ribbons, flakes, or powders, rapid quenching is required. The nucleation of crystalline phase can be prevented at a high cooling rate. In recent years, many methods to produce amorphous alloys have been reported. With the third element added into the original binary system, the cooling rate for fabricating amorphous alloys can be lowered from 10^7 K/s to 10^3 K/s. Because of the increasing demands for light and strong materials which can resist the severe environment, bulk metallic glasses (BMGs) have been developed.

In general, the vacant space among atoms in metallic glasses is called free volume. A shear localization occurs at the sites with a high amount of free volume. Amorphization of metallic material might result in excellent properties due to the atomic structure of amorphous phase, such as lower Young’s modulus, better tensile strength, higher electric resistance, and excellent gas absorption ability, which is different from the corresponding crystalline alloys.

Recently, metallic glasses are regarded as potential materials, and can be used as a coating, in an attempt to strength the substrate due to the unique physical and mechanical properties. The fundamental properties and application field of metallic glasses are listed in Table 1-3 [7]. Ternary and multi-component BMGs with the functional applications on protective coatings were fabricated by Inoue’s group [8]. The shell of Vertu, the famous cell phone of Nokia, was coated by liquid-metal alloys. It shows better mechanical properties, good-looking shiny surface as shown in Figure 1-4 [9]. To expand the applications in the electronic products and microscaled devices, metallic glasses with excellent mechanical properties are good candidates for the thin film coating. So far, the Pd-based and Zr-based thin film metallic glasses (TFMGs) have been used for nanopatterning and microactuator, which can be seen in Figure 1-5 [10].

1-4 Status of bulk metallic glasses and thin film metallic glasses

Over the past decades, bulk metallic glasses (BMGs) have attracted extensive interests because of their characteristics, such as high elastic energy, high yield strength, good wear resistance, reasonable corrosion resistance, and good forming in the viscous state. With the development of thin film technology, thin film metallic glasses (TFMGs) were successfully fabricated by co-sputtering and alloy sputtering. The liquid quenching method operated at a cooling rate of 10^3-10^8 K/s was widely employed to prepare various types of metallic glasses. TFMGs could also be fabricated in the binary Al-Fe and Au-La systems [11, 12] at a sufficient fast cooling rate (above 10^8 K/s). To lower the critical cooling rate, multicomponent systems consisting of more than three elements were adopted following the empirical rules for the formation of metallic glasses. The ternary and quaternary systems, Zr-Cu-Al [13], Zr-Cu-Al-Ni [14], and Pd-Cu-Si [15] TFMGs, were successfully deposited via alloy sputtering process.

In the past decade, the composition for forming metallic glasses was a very time-consuming process. With the sputtering process, the amorphous structure of the films can be well controlled, and thus the sputtering process can eliminate the time-consuming selection of glass forming composition. It can be expected that the amorphization of the films will be beneficial to the physical and mechanical properties. Moreover, the smoother and shinier surfaces can be obtained. Recently, TFMGs have been extensively applied to the fields of semiconductor industry, and micro-electromechanical systems (MEMSs). The metallic glasses which would become the viscous flow state in the supercooled liquid region (SLR), and TFMGs will form any shape easily upon heating at the SLR temperature [16]. After forming, the cooled TFMGs can still maintain their excellent properties of amorphous structure. The thermoplastic forming properties of TFMGs will be a promising material for use of microforming and microreplication.

1-5 Motivation

Nowadays, Mg alloys are extensively used in industrial and commercial products due to their specific strength and low cost. The light weight of Mg alloys makes it practicable that cell phones can be carried conveniently. The electromagnetic shielding capability of Mg alloys plays important role in cell phone industrial, which can protect human body from electromagnetic wave damage. However, the lower strength to resist intense stress limits the engineering applications of Mg alloys. If the problems of lower hardness and lower strength can be solved, Mg alloys will be more promising in commercial uses.

From a viewpoint of low-weight alloy with the high hardness and strength, it is noted that TFMGs coated on Mg alloy is a good candidate. In the past decade, many rigid ceramic thin films with a crystalline structure were usually used to be as a modified coating for the improvement of hardness or wear resistance [17]. TFMGs with an amorphous structure can also be employed for the achievement of hardness enhancement. Compared with the ceramic thin films, the amorphous structure of TFMGs without crystalline defects, like grain boundary, could make sample surfaces smooth and shiny, resulting in valued aesthetic appearance. Moreover, ceramic materials always exhibit a drawback of brittle nature. Once rigid ceramic thin films are subjected to overloaded force, crack opening will be triggered, and thus the coating tend to fragment into several pieces by catastrophic fracture without noticeable ductility. TFMGs can possess ductility rather than the stubborn brittle nature of ceramic thin films,. The above properties make TFMGs attractive for many applications, including electronic, medical, and surface coating.

The AZ31 magnesium alloys were selected as the raw substrates. In a view of ductile metallic glass with a high glass forming ability, we note that the ternary Pd-Cu-Si alloy systems may be good candidates for preparing the TFMGs. It is uneasy to control the composition for co-sputtering. In an attempt to obtain accurate composition of the Pd-Cu-Si TFMGs, alloys target is selected in the sputtering process. In this study, the AZ31 Mg alloys coated with the Pd-Cu-Si TFMGs are prepared and analyzed in terms of the mechanical properties.

In sputtering process, the thickness of film is a function of the deposition time. In our general senses, the thicker the film is, the more rigid in nature the film will be. However, once the thickness of the deposited film is over a critical value, the films will readily be peeled off form the substrates. On the contrary, the film with a very thin thickness would contribute little to its underlying properties. Therefore, it is crucial issue that the suitable thickness of the film can satisfy a good coherence to the substrate. The effects of various thicknesses in the Pd-Cu-Si are investigated. We compare these types of TFMGs with different indentation depth to various thicknesses, and discuss the difference in mechanical behavior.

Chapter 2　Background and literature review

2-1　Applications of Mg alloys

Mg alloys have become one of the most popular materials in industry ever since Mg element was discovered by Davy in 1808. Due to the tendency of light weight utilization and environmental consciousness, Mg alloys were widely used for structural utilization, especially in the fields of transportation vehicles. For the light weight goal, it is necessary to adopt the light metals in the components of vehicles [18]. According to the advantages mentioned in chapter 1, Mg alloys can be regarded as promising materials to replace Al alloys or plastics on the applications of electronic products and important structural materials.

Owing to the hexagonal closed-packed (HCP) structure, Mg alloys show poor workability. Thus, the shaping of Mg alloys needs adopting the die casting, thixomolding [19] or thixocasting [20]. The improvement in the workability of Mg alloys will be important for the purpose of promoting mass production of Mg alloys in the engineering applications.

2-2　Mg alloy systems

The main application of Mg metals and Mg alloys can be divided into structural applications and non-structural applications. In structural applications, there are several systems based on various alloy compositions for conventional cast.

Take some Mg alloys systems for examples. In the Mg-Al-X systems, Mg-Al-Zn, Mg-Al-Mn, Mg-Al-Si, and Mg-Al-RE (rare earth elements) series have been widely investigated. For the Mg-Al-Zn series alloys, Zn plays the role in strengthening. For example AZ91D show a good mechanical performance, castability and corrosion resistance. The ductility of Mg-Al-Mn series alloys can be improved by the addition of Mn. For the Mg-Al-RE series alloys, AE42 show the improved creep resistance, ductility, and corrosion resistance. Moreover, it is indicated that the addition of Ca in AZ series alloys can make the grain smaller to improve yield strength because of the Al_2Ca and β-$Mg_{17}Al_{12}$ phases formed on the grain boundaries [21, 22].

In the Mg-Zn-X systems, the Mg-Zn-Zr and Mg-Zn-RE series alloys have been commonly used. For the Mg-Zn-Zr series alloys, the ability of grain refinement in the Mg-Zn alloys contributed to the ZK51 and ZK61 alloy products, which exhibit a high yield stress and good casting ability. For the Mg-Zn-RE series alloys, ZE33 and ZE41 exhibit a good creep resistance. In addition, they were extensively used for the casting in elevated temperature. In the Mg-Th-X systems, the addition of Th can contribute a good creep resistance to Mg alloys. For the Mg-Th-Zn series alloys, the addition of Zn can increase the creep resistance of Mg alloys. Zh62A is a famous family of Mg alloys because it exhibits relatively high strength at room temperature.

Finally, in the Mg-Ag-X systems, the Mg-Ag-RE series are mostly popular. In the Mg-Ag-RE series alloys, QE22 is widely used for the aerospace applications. Besides the addition introduced above, there are still some often used. For instance, yttrium (Y) and rare earth element can enhance creep resistance to the QE series alloys after fully hardened by means of the T6 thermal treatment [23]. It is found that the properties of various Mg alloy systems depends on the addition of various alloys elements according to different demands for applications.

2-3 Fabrication of amorphous alloys

In the past twenty years, many techniques for fabrication of amorphous alloys have been developed. The process can be classified into three main groups according to the difference in cooling rates. The first one is forming amorphous alloys from gaseous state to solid state. This process can be carried out by sputtering and evaporation in a high vacuum environment.

The second one is forming amorphous alloys from the liquid state to solid state. By means of the temperature difference between the target and substrate, sufficient cooling rate for quenching can be achieved. The third one is forming amorphous alloys from solid state to solid state by a variety of plastic deformation, such as ion beam mixing, mechanical alloying (MA) and accumulative roll bonding (ARB) [24]. The three groups will be discussed in the following chapters.

2-3-1 Cooling from gaseous state to the solid state

The amorphous alloys can be fabricated by depositing alloys or metal elements with gaseous phase on the substrate with a relatively high cooling rate of 10^{10}-10^{12} K/s. The processes of sputtering and vacuum evaporation belong to this method [25], as illustrated in Figure 2-1 [26].

In the sputtering process, a high voltage is added to electrodes to create an electronic field, and electrons are accelerated and emitted from the cathode. After gas molecules are ionized, the metal or alloy vapors will be deposited on the substrate to form amorphous thin film while the target is impacted by the gaseous ions. In order to achieve a sufficient cooling rate, liquid nitrogen or helium is used in the cooling process.

In 1954, Buckel [27] synthesized amorphous films composed of pure Ga and Bi. The thermal evaporation impact the substrate which was maintained at a liquid helium temperature with a cooling rate above 10^{10} K/s. Subsequently, in 1986, Cotts et al. [28] fabricated the Ni-Zr multilayer thin films with the magnetron sputter method. The amorphization was successfully observed by using a differential scanning calorimetry (DSC). With the development of these techniques, cooling from gaseous state to solid state has been a common way to fabricate amorphous films. Moreover, co-sputtering deposition process [29] and alloy sputtering deposition process [13] are also adopted to synthesize multi-component monolayer TFMGs.

2-3-2 Cooling from liquid state to the solid state

Liquid quenching at a cooling rate of 10^3-10^8 K/s provides another way to fabricate amorphous alloys. Amorphous alloys can be made into different forms by the liquid quenching method, inclusive of splat quenching, melt spinning, two rollers quenching, planar flow casting, metallic mold casting, spray forming, and high-pressure die casting [30-33]. In the process of fabrication, after the alloys are atomized or melt, they will be quenched on substrate with relatively high thermal conductivity or on a low-temperature mold with a water-cooling system. By means of this method (gun quenching), the first amorphous metal Au-Si was fabricated by Klement et al. [34] in 1960.

2-3-3 Transformation from solid state to solid state

The ways of transformation from the solid state to solid state include severe plastic deformation, solid-state reaction, particle bombardment, and solid-state interdiffusion. The cooling rate becomes no more important in the process. The severe plastic deformation leads to the grain size refinement and the lattice rearrangement. As long as the grain size becomes small enough, the crystalline structure will turn into amorphous structure. In order to carry out such a large amount of plastic deformation, the ways of cyclic extrusion or cyclic compression, torsion straining under high pressure, equal channel angular pressing (ECAP), mechanical alloying (MA), and accumulative roll bonding (ARB) were commonly adopted [35-40].

According to the principles of particle bombardment, as long as the alloy surface is impacted by the heavy ions or electrons with high energy, the structure of alloy surface will be rearranged to amorphous state. The processes of neutron and ion particle bombardment irradiation, electron beam radiation, ion implantation, and ion beam mixing are all based on the same concept.

In the reaction of solid-state interdiffusion, atoms in different metal layer can diffuse through the interface to reach amorphous state under appropriate heat treatment. However, when the temperature of heat treatment is not high enough, the intermetallic compound will be formed.

2-4 Characteristics of amorphous alloys

2-4-1 Glass forming ability (GFA)

In order to make the amorphous alloys extensively applied for industry, it is essential to understand their natures. Among the factors in developing the metallic glasses, the glass forming ability (GFA) play a critical role in glass forming. GFA is the key to design and develop new metallic glasses systems [41], and it is determined by tow parameters, the critical cooling rate (R_c) and maximum attainable size (D_{max}). The formation of glass will be easier and more controllable when GFA is higher. Thus, larger D_{max} or smaller R_c is preferred to acquire higher GFA. Since D_{max} significantly is dependent on process of fabrication, and R_c is difficult to measure, several models and theories have been proposed for discussing the reliable criteria for GFA in various metallic glasses systems. These established models are based on the principles of atomic packing or thermodynamic parameters. Such models as structural models [42], theory of nearly free electron [43], chemical factors [44], phase diagrams features [45], model of solid solution [46], and atomic size criterion [47] make it possible to estimate the GFA of MGs. The kinetics is not taken into consideration [48] in the approaches above. Due to the difficulty in quantification, these approaches are limited for applications. Therefore, several GFA criterions that can be easier to quantify have been developed. Recently, the γ parameter has been viewed as reliable criteria.

2-4-2 Recently developed GFA criterions

In addition to γ parameter, researchers are dedicated to developing new indicators for describing the GFA of metallic glasses. Fan et al. [49] demonstrate a dimensionless criterion, γ, represented by $T_{rg}(\Delta T_x/T_g)^a$. Chen et al. [50] propose another criterion, δ, expressed by $T_x/(T_l - T_g)$. Many researchers consider that the criterions should be updated with the development of new metallic glasses systems because these criterions may be inappropriate to the new systems. Hence, the GFA criterions must be modified with time. After the previous argument stated by Lu and Liu [41, 51], a modified γ parameter, defined as $\gamma_m = (2T_x - T_g)/T_l$, has been proposed by Du et al. [52] in recent years.

The parameter, γ_m reflects T_g, T_x and T_l based on the measurement of GFA. Since these relevant factors can be correctly obtained during the formation of metallic glasses, the parameter, γ_m displays the best correlation with the GFA, especially for BMGs. Among this relationship, the statistical correction factor R^2 of γ_m can be consistent with various GFA parameters. The parameter, γ_m is more reliable than the previous ones. Moreover, it is easier to acquire exacter experimental data for the related factors by DSC and DTA. Thus, the parameter, γ_m become a useful and friendly tools for expressing the GFA of metallic glasses.

2-5 Empirical rules for forming amorphous alloys

The formation of amorphous phase in a binary system has much to do with the specific compositions around the deep eutectic points. A schematic drawing of binary phase diagram is shown in Figure 2-2 [53]. For composition 1, the melting state passes liquidus line at a higher temperature (point a). As the melt is cooled down, it will go through a larger temperature range. The crystallization and growth may occur before reaching T_g. For composition 2, the melting state passes liquidus line at a lower temperature (point b). Since the temperature range between T_l and T_g is small, the thermal energy for crystallization will become lower. In conclusion, the composition of binary system quenching at the temperature around the deep eutectic points will lead to a lower T_l, and thus, the GFA of metallic glasses can be enhanced.

The first amorphous alloys were successfully fabricated around 1960s [34]. Subsequently, various techniques were developed to synthesize BMGs empirically. Gradually, researchers found that the amorphous alloys could be fabricated at critical cooling rates as low as 1-100 K/s for specific elemental constituents. With the development of various amorphous alloy systems in the past decade by Inoue's group, three basic empirical rules for BMGs designs with high GFA [7,54-56] have been proposed. These empirical rules are listed as below: (1) multicomponent systems composed of at least three elements, (2) difference in atomic size more than 12% among the main constituent elements, and (3) negative heats of mixing among the main constituent elements.

The difference among atomic sizes for more than three elements system will hinder the motion when the system is quenched from melt to a solid state. As long as the difference in size among the main constituent elements is larger than 12%, the GFA of amorphous alloys increase with increasing categories in multicomponent systems. After quenching, the short-range-ordered structure will be formed in a high dense packing arrangement. In Hume-Rothery criterion [53], the difference in atomic size to form solid solution is less than

15%.

On the basis of the famous thermodynamic equation $\Delta G = \Delta H_{mix} - T\Delta S_{mix}$, the heat of mixing, ΔH_{mix} represents atomic bonding ability between two atoms. Larger negative ΔH_{mix} stands for weaker the atomic bonding ability of the same atoms. When the melt is quenched with a larger negative ΔH_{mix}, usually ranged from -20 to -30 kJ/mol, it will be easier for the distinct atoms to be bound together to form amorphous alloys. According to the Miedma's macroscopic model, the mixing enthalpy values of various ternary amorphous systems and three binary subsystems can be calculated, as listed in Table 2-1 [57].

The nucleation of crystalline phase and the rearrangement of atoms will be suppressed by following the above-mentioned empirical to fabricate amorphous alloys due to a higher liquid/solid interfacial energy. The lower atomic diffusivity and higher viscosity result in the difficulty in the growth of crystalline phase. These mechanisms for forming BMGs shown in Figure 2-3 [7] consist in three characteristics for a particular liquid structure.

2-6 Physical vapor deposition

2-6-1 Introduction of sputtering

Sputtering deposition is a physical process involved in ion bombardment and momentum transfer to fabricate thin films. In the deposition process, the incident particles with high energy impact the surface of the target, resulting in the bond breaking and atoms dislodging. It is assumed that elastic collision occurs when the incident particles hit the target due to almost no loss in momentum transfer.

Generally, sputtering deposition should be operated in: (1) a good vacuum environment ($<10^{-5}$ torr); (2) a low pressure gas environment. When the sputtered particles emit from the target to the substrate, no gas phase collision happens in a low pressure gas environment. Once any particle starts hitting the substrate surface with sufficient energy to break bond and dislodge atoms, the sputtering process occurs. The parameter of sputtering yield is the ratio of atom sputtered to the number of incident particles with sufficient energy [58], and it is closely related to the mass of the bombarding particle as well as its energy.

The illustration in Figure 2-4 [58] shows that when the bombarding particles collide the surface, they penetrate in ten near-surface region. More than 95% transferred energy dissipates in form of heat near the surface region. Similar to elastic collision, some bombarding particles show are reflected as high energy neutrals, while some behaving as complete non-elastic collision are implanted in the surface.

The diluted Ar gas is poured into the ultra-high vacuum chamber. The gas Ar molecules will be ionized to Ar^+ as long as bias between anode and cathode becomes large enough. The incident particle, which is also called plasma, is produced by glow discharge. The electrons produced at the beginning of glow discharge are called primary electrons. The primary electrons are accelerated by the electric field. When discharge occurs, the primary electrons collide with gas molecules, resulting in the generation of the positive ions. After that, the positive ions bombard the cathode surface, and thus, the secondary electrons are generated. With the secondary electrons, the efficiency of gas ionization will be increased, and the self-sustained discharge [59] will be generated.

Sputtering deposition provides an easy way to control the film thickness and refine the surface roughness. Moreover, the excellent uniformity of film over large areas can be acquired by employing the sputtering techniques. Hence, sputtering deposition has been extensively used for surface refinement in industry.

2-6-2 DC and RF sputtering

In DC (direct current) diode sputtering, the electrons are emitted and accelerated away from the cathode. However, it is not an efficient way to sustain the discharge. By controlling the magnitude and the arrangement of the magnetic field appropriately, the electrons can be deflected to stay near the surface of the target. The high density plasma is created by the high flux electrons. The ions are extracted from the plasma to the sputtered target producing a magnetron sputtering configuration. In RF (radio frequency) sputtering, the power supply works at high frequency. Different from DC sputtering, RF sputtering can handle insulating materials even if the sputtering yield is low. In a word, RF sputtering can provide stable power to dielectric targets. The major advantage both the DC and RF magnetron sputtering configuration possess is no energy loss attributed by physical and charge-exchange collisions. Therefore, DC and RF magnetron sputtering configuration exhibit a higher sputtering rate with a lower potential on the target compared with the DC diode configuration.

2-6-3 Nucleation and growth of thin films

Many properties of film, such as grain size, surface morphology, and film density are dominated by the nucleation and the growth of the film. In terms of film growth, several essential aspect are listed below [58]: (1) substrate surface roughness; (2) surface temperature; (3) adatom surface mobility; (4) geometrical showing effects (angle-of-incidence effects);

and (5) reaction and mass transport during deposition such as segregation effects and void formation.

As thin film grows, the substrate surface morphology changes due to the faster growth of some features or crystallographic planes. Hence, the surface roughness will be increased. The adatom surface mobility increases with increasing surface temperature. As long as the flux of deposition on the substrate exceeds that of leaving, the nucleation and growth of the film will start. The energy absorption between the adatoms and substrate dominates the nucleation process. In addition, the surface diffusion energy affects the binding and migration of the deposited atoms [60]. Indeed, the migration of atoms is not randomly distributed. It is related to crystallographic directions and surface topography of the substrate. Besides, atoms mobility induced by temperature can also affect the migration. Basically, the three common modes of film contain island (or Volmer-Weber) mode, layer (or Frank-Vander Merwe) mode, and Stranski-Krastanov mode [61]. These modes are illustrated schematically in Figure 2-5 [61].

The island mode results from the nucleation of the most instable cluster on the substrate. The atoms and molecules are bound more tightly than the atoms and substrate. Moreover, the growth mechanism leads to the three dimension island. Such metallic glasses on insulators as alkali halide crystals, graphic, and mica substrates can be classified in this mode. For layer mode, the film grows layer by layer in two dimensions when the binding between coating atoms to substrate is stronger than that between coating atoms. In the beginning, the atoms condense as a single monolayer and no energy barrier is there for nucleation. The growth mode is common especially for heteroepitaxial thin film growth in semiconductor-semiconductor systems and some metal-metal systems. The mechanism of Stranski-Krastanov mode is the combination of the island mode and the layer mode.

2-6-4 Growth of amorphous films

Amorphous films with short-range order can be fabricated by several techniques [69]: (1) deposition of a natural glassy material; (2) deposition of complex metal alloys; (3) deposition at low temperatures that make the mobility insufficient to form crystalline structures; (4) ion bombardment during deposition; (5) ion bombardment of films after deposition; and (6) deposition of materials, whose bonds are partially saturated by hydrogen such as a-Si:H, a-C:H and a-B:H [62, 63].

2-7 Properties of TFMGs

2-7-1 Thermal properties

As mentioned above, metallic glasses display special thermal properties such as broad SCLR. At the SCLR, most metallic glasses show a viscous flow. The formability of MGs can be improved due to the viscous flow. This thermal property makes TFMGs be used as the three-dimensional MEMS. In order to measure the thermal properties exactly, the working temperature should be confirmed. After that, heat treatment such as annealing process should be carried out. Thus, the thermal properties and SCLR of TFMGs are usually measured by differential scanning calorimetry (DSC).

From the thermography trace of DSC result (Figures 2-6 and 2-7) [15, 64], the glass transition temperature (T_g), crystallization temperature (T_x) and SCLR ($\Delta T_x = T_x - T_g$) can be determined according to the changes of the slops. For the Pd-TFMG, the T_g, T_x and ΔT_x are determined to be 637 K, 669 K and 32 K, respectively. For Zr-TFMGs, its T_g, T_x and ΔT_x are 643 K, 713 K and 70 K, separately. Because Zr-TFMG exhibits an endothermic reaction, the slop changes due to glass transition at about 643 K. Moreover, an exothermic reaction is owing to crystallization at about 713 K, as shown in Figure 2-8 [64].

In the time-temperature-transformation (TTT) diagrams which also conducted by using

DSC, the thermal stability of the THMGs can be represented. From two typical TTT diagrams of TFMGs, as shown in Figures 2-8 and 2-9 [64], the time till the onset of crystallization and amorphization can be observed. Besides, the allowable interval of the temperature and the heating time can also be ensured for the micro-forming process and annealing heat treatment.

2-7-2 Mechanical properties

With the development of BMGs, their mechanical properties of have been extensively studied for a long time. The superior mechanical properties of BMGs are the reasons why they have a variety of applications. From the view of structure, BMGs display the dense packing and randomly atomic arrangement configuration. Thus, the displacements of amorphous alloys are limited when an external stress is applied. Without dislocation mechanisms for plastic deformation, the amorphous alloys therefore exhibit some unique properties such as high strength, hardness, Young’s modulus, and good fracture toughness. However, these superior mechanical properties as mentioned above are not completely performed in the TFMGs for some reasons. For instance, because the sample sizes of TFMGs are different from those of the BMGs, the testing methods for BMGs are difficult to directly performed on TFMGs. Therefore, the properties of TFMGs should be measured by the sensitive instruments and careful methods. Furthermore, the testing of bulk material exhibits the average properties over a large section. However, the testing of thin film material displays the localized and specific properties in a small scale due to the limit of measurements. For the reasons above, the microtester or sensitive instrument, such as nanoindenter, will be a safe way to analyze the TFMGs.

For example, the Zr-based TFMGs with micro-scale thicknesses on silicon substrates are analyzed by nanoindentation techniques. The nanoindentation-hardenss-measurement results of the as-deposited and the annealed films as a function of composition on the $Zr_xCu_{(1-x)}$ TFMGs are shown in Figure 2-10 [65]. It is shown that the moderate Zr concentrations (45 – 65 at %) would result in relatively high hardness (~7 GPa) and Young's modulus (~125 GPa) for the annealed films. In addition, the relationship between Vickers hardness (H_v) and Young's modulus is also shown in Figure 2-11 [7]. In comparison with these two types of the Zr-based metallic glasses, both of the the hardness and Young's modulus of the Zr-based TFMGs are slightly higher than those of bulk BMGs.

In terms of the deformation mechanism, the amorphous alloys are quite different from the crystalline alloys. In crystalline alloys, once the external shear stress exceeds the critical resolved shear stress on a slip plane, the plastic deformation will occur. Meanwhile, the dislocations are formed, and then start to glide along the slip direction on a slip plane. Thus, in crystalline materials, the mechanical properties have much to do with the crystal and electrical structures. On the other hand, no slip system exists in amorphous alloys due to the lack of long-range-order structure. Their plastic deformation is operated by the mechanisms of shear bands.

The amorphous alloys display short-range-order structures. The small spaces called free volumes exist in the structure, as shown in Figure 2-12. Recently, several theories have been proposed to describe the heterogeneous plasticity in MGs. The plastic flow in amorphous alloy is viewed as a diffusion-like process. This is involved in the stress-induced self-assembled of smaller unit of plasticity called flow defects or shear transformation zones (STZs) [66, 67]. STZs are the fundamental unit of plasticity in a form of a small cluster of random close-packed atoms. These flow defects or STZs are associated with about 10 to 50 atoms in open spaces or free volume sites, which are distributed over the amorphous structure. The illustration of STZ deformation in two-dimensional space is shown in Figure 2-13. The dominated mechanisms in glass structure and deformation are generally localized to this mere fine scale. In other words, it is usually assumed that the plastic deformation in amorphous alloys is dominated by the amount and distribution of the free volume.

Moreover, the moving of STZ is attributed by the releasing of adiabatic heat near the STZ [68]. When more and more STZs start moving, the huge adiabatic accumulates, resulting in the raise of the temperature around the shear plane. After the temperature reach the glass transition temperature, a fluid region or fluid layer will be formed in the shear plane, as shown in Figure 2-14. The fluid region will possess more free volume sites for STZs. Thus, the amorphous alloys will be deformed more easily.

2-7-3 Chemical properties

In addition to good mechanical properties, it has been discovered that the homogeneous structures of single phase make BMGs display high corrosion resistance. That is because the amorphous structures are lack of grain boundaries, dislocations, and other crystal defects. Moreover, the corrosion resistance can further improved by adding some corrosive solutes. Take the Zr-Al-Ni-Cu amorphous alloys system for instance, when elements of corrosive solutes such as Nb, Ta, Ti, and Cr [69] are added, the corrosion resistance can be enhanced. Recently, some researches indicate that the Pd-based and Fe-based [70] amorphous alloys also exhibit high corrosion resistance. Thus, they can be used for practical corrosion resistance materials.

Chapter 3 Experimental Procedures

The $Pd_{77}Cu_6Si_{17}$ (in atomic percent) alloy films were selected to be deposited on the polished AZ31 substrates by magnetron sputtering, denoted as PCS. The structural characteristics of thin films were examined by X-ray diffraction (XRD). The film compositions were confirmed by scanning electron microscopy (SEM) with energy dispersive X-ray spectrometer (EDS). The mechanical properties of PCS were evaluated by microhardness and nanoindentation. The scratch test was operated to understand the films deformation in different depths. In addition, the wear coefficient was calculated to compare the differences among AZ31, and PCS. The flow chart of the experimental procedures is shown in Figure 3-1.

3-1 Materials

The AZ31 billets were purchased from the CDN company, Deltabc, Canada. This as-received alloy was fabricated through semi-continuous casting and showed the form of billet with 178 mm in diameter and 300 mm in length. The as-received AZ31 billets were cut into the small pieces measuring 8 mm in width, 8 mm in length, and 3 mm in thickness. The detailed chemical composition of AZ31 Mg alloy is listed in Table 3-1. The $Pd_{77.5}Cu_6Si_{16.5}$

alloy target with a purity of 99.99% was purchased from Gredmann Taiwan, corp.

3-2 Sample preparation

3-2-1 Substrate preparation

In this study, the AZ31 plate was selected as the substrate. To make the surface smoother, the substrates were grinded with abrasive paper and polished with diamond paste. To avoid impurities and greasy dirt contaminating the substrates, the following steps for cleaning the surfaces were adopted. An ultrasonic cleaner was used to clean the substrates in alcohol for 10 minutes, followed by the acetone rinsing for 10 minutes. Finally, air was employed to dry the substrates.

3-2-2 Film preparation

The $Pd_{77}Cu_6Si_{17}$ alloy (PCS) coatings were deposited on the smooth AZ31B substrates by a single-gun magnetron sputtering system using $Pd_{77.5}Cu_6Si_{16.5}$ alloy target of 50.8 mm (2 inches) in diameter.

The main chamber was pumped down to a base pressure less than 1×10^{-6} torr by a cryo-pump. The $Pd_{77}Cu_6Si_{17}$ alloy target was located on the DC gun with a power of 200 watt, and pure argon atmosphere as the working gas was maintained at the rate of 30 standard cubic centimeters per minute (sccm). The substrate was rotated at an average speed of 10 rpm for ensuring uniform distribution of film thickness. The working distance between the holder and the DC gun is 120 mm. With appropriate time for sputtering, PCS thin films were deposited on the AZ31 substrate with various thicknesses of 30, 50, 100, 200, 300, 500, 1000 and 2000 nm. These specimens are denoted as PCS-30, PCS-50, PCS-100, PCS-200, PCS-300, PCS-500, PCS-1000, and PCS-2000, respectively.

3-3 Property measurements and analyses

The film structure was characterized by Bede D1 HR-XRD grazing incidence in-plane X-ray diffraction (XRD), and the film compositions were confirmed by JEOL-6400 scanning electron microscopy (SEM) linked with energy dispersive X-ray spectrometry (EDS). The glassy nature of as-deposited $Pd_{77}Cu_6Si_{17}$ thin films was characterized by Bede D1 HR-XRD grazing incidence in-plane X-ray diffraction (XRD), and the film compositions were confirmed by JEOL-6400 scanning electron microscopy (SEM) linked with energy dispersive X-ray spectrometry (EDS). The films deposited on P-type (100) silicon wafers and deposited on AZ31 Mg alloys were both examined by XRD.

3-4 Microhardness tests

The difference in hardness between the AZ31 Mg alloys and AZ31 Mg with the $Pd_{77}Cu_6Si_{17}$ amorphous coatings was examined by using microhardness test. The microhardness tests of samples were conducted using a SHIMADZU HMV-2000 Vickers Microhardness Tester with various loads from 10 to 100 g for a fixed duration time of 10 seconds. The hardness values of each sample were averaged from 30 datum points chosen randomly. The microhardness data was analyzed to inspect the hardness change.

3-5 Nanoindentation tests

For comparison of hardness with different testing instruments, all the coating samples were also measured by the MTS XP nanoindenter system via the continuous stiffness measurement (CSM) mode. The nanoindentation testing was executed with a maximum load of 500 mN (Figure 3-2). The Berkovich tip was a three sided pyramid with a geometrical symmetry. There existed a flat profile with a centerline-to-face angle of 65.3 degrees. Nanoindenter is very sensitive to the external environment and the flat condition of sample surface. It would be necessary to keep clean and dry surface of thin films before nanoindentation test. In the analysis of nanoindentation test, the indented depth is set from the shallow up to the deeper regime (double of the film thickness) in order to obtain the average hardness contributed by the Pd-Cu-Si thin film and the AZ31 substrate.

3-6 Observation of indentation marks

After conducting the microhardness and nanoindentation tests, JEOL-6700 Field-Emission SEM was used to examine the surface conditions of the indented thin films. The morphology of indentation marks was observed. In addition, the hardness in microhardness test was calculated based on the measurement of indentation marks under SEM observation.

Chapter 4 Results and Discussions

4-1 Amorphous nature

To identify the structural characteristic and composition, the as-deposited $Pd_{77}Cu_{6}Si_{17}$ thin films on the AZ31 Mg alloy or Si substrate were identified by XRD and SEM/EDS. According to the EDS results, all compositions of the as-deposited Pd-Cu-Si thin films are close to $Pd_{77}Cu_{6}Si_{17}$, as indicated in Table 4-1, implying that almost no side-reaction occurs.

Based on the XRD results, Figure 4-1 (a) shows the XRD pattern of the AZ31 substrate, indicating three major peaks of $(10\bar{1}0)$, (0002), and $(10\bar{1}0)$. The as-deposited $Pd_{77}Cu_{6}Si_{17}$ thin films on silicon substrate present a broad diffraction hump characteristic of amorphous nature without distinct crystalline peaks, as shown in Figures 4-1 (b). Figure 4-2 shows the XRD pattern of the 2000 nm $Pd_{77}Cu_{6}Si_{17}$ thin film deposited on the AZ31 substrate. The amorphous signal consisting of a hump located at the diffraction angle range of 35^{o} to 50^{o} is detected with three major peaks of the AZ31 substrate. These results reveal that the nature of the as-deposited thin films does not change substantially with the change of substrates.

To sum up the results above, the as-deposited $Pd_{77}Cu_{6}Si_{17}$ thin films is glassy structure.

Moreover, the interface between amorphous coating and the AZ31 substrate seems to be tightly bound through physical contact, since no obvious crystalline diffraction peak of any reactive phase formed by the reactions is observed.

4-2 Microhardness and Nanoindentation tests of $Pd_{77}Cu_6Si_{17}$ TFMGs on AZ31

Before the microhardness test, the roughness and surface topography of the AZ31 substrate were examined using atomic force microscopy (AFM) as shown in Figure 4-3 (a) and Figure 4-4 (a). The roughness (Ra) is ~70 nm and ~10 nm under surface treatments of diamond paste polishing and SiO_2 polishing, respectively. Figure 4-3 (b) and Figure 4-4 (b) are their morphologies taken by optical microscopy (OM). Despite the difference in roughness, the substrates exhibit almost the same hardness in microhardness test. The hardness is insensitive to the 10-70 nm roughness in this range under microhardness testing.

Although it is easier to prevent the samples from pollutions, surface oxidation of the AZ31 substrate is unavoidable in the procedure of mechanical polishing. In our previous results [71], the hardness datum base for the AZ31 substrate has been set up. Taking some parameters into the Hall-Petch relationship, the hardness can be well followed using the following equation:

$$H_v = 40 + 72\ d^{-\frac{1}{2}}, \qquad (4\text{-}1)$$

where H_v is the hardness, and d is the average grain size. The average grain size of the current AZ31 substrate estimated from Figure 4-5 is ~60 μm. Taking the average size of ~60 μm into the equation 4-1, H_v is 49. The measured hardness of the AZ31 substrate after mechanical polishing is ~53 H_v, which can be transformed into 0.52 GPa. It could be inferred that the oxidation of the AZ31 substrate also had no strong effect on hardness.

Microhardness testing provides a simple way to examine if the TFMGs would toughen the AZ31 substrate. The cracks of PCS resulted from the applied loads may cause unclear indentation marks under OM observation. The high-resolution measurement for indentation mark can be accomplished under SEM observation. To obtain the accurate hardness values of TFMGs, we measured the indentation marks of the deformed samples and estimate the hardness based on the standard hardness equation. The equation of Vickers microhardness measurement can be expressed as [53],

$$H_v = 0.102 \times \frac{F}{S} = 0.102 \times \frac{2F/\sin(\alpha/2)}{d^2}, \qquad (4\text{-}2)$$

where F is the applied loading, S is the area of indentation mark, α is the face-to-face angle, equal to 136^o of Vickers tip, and d is the average length of the diagonal lines caused by tip, respectively. Using the value of d accurately measured from SEM observation and all known parameters, the hardness can be calculated.

For the convenience of expressing the indented behavior, the penetration depth of indent (*d*) over the film thickness (*t*), namely, *d/t*, is denoted as β. For the microhardness test, the ratio is more than 1 for all the cases, from 1.25 up to 11. For nanoindentation, β varies from 0.05 to 2.0. The hardness measurements and percentages of enhancement from microhardness and nanoindentation tests are shown in Figure 4-6, 4-7, and 4-8.

When the penetration depth is limited in the shallow region, the enhancement of apparent hardness can be more than 100% due to the protection of hard TFMG. Subsequently, the hardness decreases with increasing β ratio. In the β range between 1 and 2, hardness drops down rapidly because of the rising contribution of AZ31 substrate. The enhancement of TFMG to the whole material becomes less and less. When β is over 2.0, the hardness of the AZ31 substrate starts to dominate the whole system. As a result, the decreasing tendency of hardness slows down in the range of $2.0 < \beta < 11$, approaching to the hardness of AZ31 substrate gradually. It is noticed that the two microhardness-β curves for PCS-1000 and

PCS-2000 match well, as shown in Figure 4-6. The current results demonstrate that the hardness of coated specimen is insensitive to the thickness of TFMGs. The β ratio appears to be the key parameter in determining the system hardness.

For nanoindentation, the indented β ratio is limited within 2.0 as shown in Figure 4-7. Due to the dominant role of TFMG, the nanoindentation hardness readings are mostly higher than 2 GPa, significantly higher than the AZ31 substrate, 0.52 GPa. Though the indenter tips for microhardness and nanoindentation are not the same, the trends of hardness-β curves obtained from these two test are still combined for comparison, as presented in Figure 4-8. It is evident that the basic variation trend of the hardness as a function of β ratio from the nano to micron range is similar.

4-3 Hardness marks of $Pd_{77}Cu_6Si_{17}$ contings on AZ31

The indentation mark of AZ31 substrate is shown in Figure 4-9. We here use the PCS-2000 as the example to demonstrate the indented surface morphology. PCS-2000 at β~1.25 exhibits another type of morphology, as shown in Figure 4-10 (a). Compared with the AZ31 substrate, the surface becomes smoother after coating. Based on the inclined sides of the microhardness marks in Figure 4-10 (a), the PCS TFMGs may provide the fracture resistance during deformation. At β~2, a small number of shear bands are found in some of the marks, as indicated in Figure 4-10 (b). The formation of shear band indicates the PCS TFMGs deform with an inhomogeneous plasticity.

The formation of shear bands in the microhardness marks increases with increasing β ratio. In the case, propagation zone with shear bands at β~2.5 can be easily observed. The propagation zone of shear band is along the directions out of the mark, as shown in Figure 4-11. At this stage, there is still no crack observed in all the marks. At β~3.5, the shear bands can be observed even more easily in most marks, as shown in Figure 4-12. When β~5, shear bands are observed obviously as shown in Figure 4-13. The spaces between shear bands become much closer, and the widths of shear bands become finer. Figure 4-14 (a) shows the enlarged image taken from Figure 4-13, indicating the small crack caused by particles. In Figure 4-14 (a), it shows that the particles with size of ~1 μm will block the propagation of shear bands. Since the shear bands are hindered, the stress released by propagation will concentrate around the particles. Once the concentrated stress is over a critical value for the PCS TFMGs, the cracks will be induced. Several cracks are found, but the cracks are all limited just around the particles. In Figure 4-14 (b), the enlarged view exhibits the finer shear bands.

For PCS-1000, β~3, shear bands are observed spreading over the entire area in the most SEM images, as shown in Figure 4-15. There is no crack observed in all SEI images. When β~5, some cracks are found in the mark, as shown in Figure 4-16. The morphology and the position of crack are quite similar to that of the PCS-2000 at β~5. The above two results are consistent with the dependence of hardness as a function of β in Figure 4-8. The similar morphology and the same deformation mechanism further prove the hypothesis, i.e. the ratio of β is a key point to determine the hardness of the system instead of only film thickness.

In some cases for PCS-1000, at β~8, the crack is not only formed around the particles, but also starts to propagate along the shear bands, as shown in Figure 4-17. However, most of the images show no crack, or cracks just around the particles. It means that the PCS-1000 can still resist the load of 50 g. When β~11, the cracks can be observed easily as shown in Figure 4-18 (a). Based on all the images with cracks, it is deduced that when the load increases to a critical level, the particles will play an important role in the deformation of the PCS TFMGs. If there are not many particles with size of ~1 μm, crack will disappear in the marks, as shown in Figure 4-18 (b). This result suggests that the particles with size of ~1 μm will result in the crack propagation with increasing loads if many particles in such size are there. Once the crack propagation becomes the dominant role, the film will peel off easily. For the samples applied at a larger load, surface condition will dominate the deformation morphology of samples.

The indentation depths for PCS-1000 and PCS-2000 are over the film thickness in microhardness test, i.e. $\beta>1$ in all cases. The formation of shear bands increase with increasing loads. Most of the films show no crack but shear bands. It can be concluded that the shear bands formed in metallic glasses provide a moderate deformation. The PCS TFMGs deposited on AZ31 can enhance the hardness, and the mechanism of shear bands prevents the film from cracking, at least in the range of $\beta < 5$.

The nanoindentation mark of PCS-2000, β~2, is shown in Figure 4-19. The size is about to that of PCS-2000 at β~2.5 in microhardness test. In Figure 4-19, it is found that the nanoindentation mark is very clear, and no crack is observed in the mark. Some shear bands appear just at the left side of the mark. In fact, shear bands can be observed at all the sides of the mark, emerging inside and outside the mark, as indicated in Figure 4-20 (a) and Figure 4-20 (b).

The nanoindentation mark of PCS-1000 is shown in Figure 4-21. The size is a little smaller than that of PCS-2000. It is coherent to the result in Figure 4-18. The morphologies of PCS-1000 and PCS-2000 are quite similar after deformation. Although there are some scratches in the surface of PCS-1000, the PCS TFMGs provide the fracture resistance with shear bands during deformation. It can be concluded that the shear bands formed in metallic glasses provide a moderate deformation both in microhardness and nanoindentation test.

4-4 Hardness calculation and comparison

In previous studies, various ceramic or metallic hard thin coatings have been applied for preventing damage and improving the hardness properties of substrate [72,73]. For analyzing the enhancement of hardness, the interaction between the hard thin coating and soft substrate needs to be clarified under the different conditions. In 2001, a work-of-indentation approach was extended to a general formula by Tuck et al. [74]. The hardness of each constituent andcoating thickness can be integrated and expressed by

$$H = H_s + \frac{H_f - H_s}{1 + k\beta^X} \tag{4-3}$$

Here H is the measured hardness reading, H_s is the relative minimal hardness of the substrate with the hard coating thin film at $\beta \sim 10$, H_f is the intrinsic hardness for the coated film, k is a dimensionless hardness transition parameter, and X is the power exponent depending on the deformation mode and geometry. With the above measured system hardness H, it is intended to extract the relative substrate and film hardness based on equation 4-3. Since there are more than one variables involved, we need to use the iterative extrapolation method to calculate the best fit values of H_s and H_f, etc. The details of all fitting results for various samples are presented in Table 4-2. Figure 4-22 shows the combined data from the least square curve fits to the empirical data on the PCS coatings of 200, 500, 1000, and 2000 nm in thickness, respectively, with the correlation coefficient R^2 between the model and experimental data over 0.997. The model fitting is found well in accordance with the experimental data. The measured datum points are marked with symbols and the model fit is shown by different lines. Note that the experimental data used to fit in Figure 4-22 exclude those in the very shallow regime with β less than 0.1, for the sake that these date show greater scattering. If only the average hardness readings are included, the fitting is still good. The fittings indicate that the H_s values for AZ31 substrate are located within 0.69 and 1.12 GPa, H_f values are within 6.59 to 7.98 GPa, k values within 7.08 and 22.03, and X values within 1.76 and 2.26.

For hardness values, it is expected that, as the thickness of the similar coatings increases, and hence the coating plays a more important role in the energy absorption during indentation, the hardness is expected to increase [74,75]. For the current experiment, the coatings of different thicknesses possess similar microstructures, due to the same deposition conditions. Therefore, the variations of X, k, H_s, H_f, and the measured apparent hardness H can be discussed below.

The X value represents a hardness shifting factor between the substrate and coating film with the different deformation modes, geometry, and interaction with each other. When the thin film and the substrate material are both easier to deform together at the same time (as the case of the 200 nm coating), the external pressures (indentation) can be more evenly distributed the force to the film and substrate, resulting in a smaller X value and a smoother hardness-β curve (Figure 4-22). On the other hand, as the coating is thicker over the critical thickness (as the case of the 2000 nm coating), the coated film would become an independent hard material with weaker interaction with the substrate as a separate bulk. Under applied pressure or load, the film takes most of the deformation energy by itself as a victim material. The resulting X value will be higher and the hardness-β curve will be steeper (Figure 4-22). When the fatal force cannot be afforded by the coated hard thin film, the film will be damaged or collapsed and the substrate will be exposed.

The above arguments may also be applied to the fitting parameter k value. The k value is dimensionless hardness transition parameter that will affect the second term in equation 4-3, namely, $\Delta H/(1+k\beta^X)$, where ΔH represents $(H_f - H_s)$. When k is small (as k=7.08 for the thinner PCS-200 sample), the second term will be larger, leading to a higher measured apparent hardness H, and vice versa. Meanwhile, the k value will also affect the relative contribution of the load carrying by the substrate and film. Based on the calculation in ref. [74], the hardness-β curves under a given X will shift to the right with increasing k value, meaning the film will carry a higher percentage of indented load, and the high to low hardness transition (or the deflection point in Figure 4-22) will sustain until a higher β ratio. However, this trend is not so obvious since the X value is not fixed in Figure 4-22.

As for the extracted H_s and H_f, it can be seen from Table 4-2 that, with increasing film thickness, the interaction between substrate and film becomes weaker, so that the relative minimal substrate hardness H_s gradually decreases from 1.1 GPa to 0.69 GPa, and approaches to the original AZ31 substrate hardness without coating (~0.52 GPa). Note that the extracted H_s from the does not appear to be a fixed value ~0.52 GPa from the iterative extrapolation method. This is mainly a result of the mutual interaction between the coated film and the substrate, partly due to the residual stress retained in the soft AZ31 substrate and partly due to the constraint from the film. At the same time, with increasing film thickness, the film hardness gradually increases from 6.59 GPa to 7.98 GPa, and approaches to the ideal PCS film material hardness (~8-10 GPa). This result is consistent with the previous finding [16] that the intrinsic coated film hardness (H_f) would increase with increasing coated film thickness.

From the experimental measured apparent hardness *H*, and the extracted film hardness H_f, the 2000 nm sample always exhibits the much higher readings. This might give an idea that the 2000 nm film coating would yield the best surface hardening effect for the AZ31 Mg alloy. Nevertheless, the higher *k* and *X* values of this sample reveal the weaker interaction between substrate and film, and the thicker film will carry most load and become prone to film cracking problem. For solid bonding and better plasticity of the coated film, a lower *X* and more even distribution of the applied load on both substrate and film would be a more promising selection. With this consideration, the 200 nm coatings appear to be more feasible.

Finally, it is interesting to identify the range for the optimum PCS coated film thickness. In this study, the PCS TFMG films thinner than 100 nm or less would lead to unsatisfactory film coverage. The ultra thin film would often cause inadequate surface hardness. The optimum extracted substrate relative hardness H_s is found to be around 200 nm. The predicted trend of the relative substrate hardness as a function of the surface hard coating thickness for the $Pd_{77}Cu_6Si_{17}$ TFMGs deposited on the AZ31 substrate is presented in Figure 4-23. An optimum hard coating will be highly useful for industry applications.

Chapter 5 Conclusions

(1) In this study, the PCS TFMG is demonstrated to be a promising protective film to enhance the hardness of the AZ31 Mg alloy. With proper PCS coating, the apparent measured surface hardness, and likely the surface wear resistance, can be substantially enhanced.

(2) The evolution of shear bands in the TFMG coated layer provides a moderate deformation mode in preventing the film from cracking fiercely. Based on the SEM images with local micro-cracks, it is deduced that the retained particles in AZ31 Mg would cause local cracking when the indented load reaches a critical level.

(3) Consistent with the equation derived by Tuck et al. [74], the relative indentation depth (β) appears to be the key parameter on the overall deformation mode and substrate-film interaction.

(4) Through the iterative calculations by computer software, the involved parameters X, k, H_s and H_f are extracted accordingly. As H_f increases from 6.59 to 7.98 GPa with increasing film thickness, the interaction between the AZ31 substrate and PCS TFMG film becomes

weaker, resulting in the extract relative substrate hardness H_s decreasing from 1.1 GPa to 0.69 GPa.

(5) For thinner TFMG coatings, the coated film and the substrate have the lowest X and a smaller relative hardness gap, and the applied load is easier to distribute evenly to the film and substrate. This will lead to a smoother hardness-β curve and a lower tendency of coating cracking. With this aspect, the coatings ~200 nm appear to be more feasible. Judging from all factors related to hardness/wear improvement, more even load transfer distribution, and film cracking issues, the optimum coating thickness in this study is around 200 nm.

References

[1] Y. Kojima, Mater. Sci. Forum **3**, 350-351 (2000).

[2] G. V. Raynor, *The Physical Metallurgy of Magnesium and Its Alloys*, Pergamon Press, London. (1957).

[3] T. Lyman, H. E. Boyer, P. M. Unterwesier, J. E. Foster, J. P. Hontans and H. Lawton, *Metals Handbook*, 8, ASM International, Metal Park, Ohio. (1975),

[4] R. W. Cahn, P. Hassen, E. J. Kramer, in *Materials Science and Technology Structure and Properties of Nonferrous Alloys*, VCH, New York. (1996).

[5] A. C. Lund and C. A. Schuh. J. Appl. Phys. **95**, 4815-4822 (2004).

[6] M. H. F. Overwijk, F. C. van den Heuvel and C. W. T. Bulle-Lieuwma, Vac. Sci. Technol. B **11**, 2021-2024 (1993).

[7] A. Inoue. Acta Mater. **48**, 279-306 (2000).

[8] A. Inoue, A. Kato, T. Zhang, S.G. Kim, and T. Masumoto, Mater. Trans. **32**, 606-609 (1991).

[9] J. Schroers, and N. Paton, Adv. Mater. Processes, 61-63 (2006).

[10] T. Fukushige, S. Hata, and A. Shimokohbe, J. Microelectromech. Syst. **14**, 243-253 (2005).

[11] S. Bysakh, P.K. Das, and K. Chattopadhyay, Philos. Mag. A **81**, 2689-2704 (2001).

[12] R. B. Schwarz, and W.L. Johnson, Phys. Rev. Lett. **51**, 415-418 (1983).

[13] S. Hata, K. Sato, and A. Shimokohbe, Proc. SPIE, 97-108 (1999).

[14] J. P. Chu, C.T. Liu, T. Mahalingam, S.F. Wang, M.J. O'Keefe, B. Johnson, and C.H. Kuo, Phys. Rev. B **69**, 133410-1 - 113410-4 (2004).

[15] Y. Liu, S. Hata, K. Wada, and A. Shimokohbe, Jpn. J. Appl. Phys. **40**, 5382-5388 (2001).

[16] G.P. Zhang, Y.D. Liu and B. Zhang, Scripta Mater. **54**, 897-901 (2006).

[17] H. Hoche, H. Scheerer, D. Probst, E. Broszeit and C. Berger Surf. Coat. Technol. **174–175**, 1018-10323 (2003).

[18] H. Friedrich and S. Schumann, J. of Mater. Proc. Technol. **117**, 276-281 (2001).

[19] 葉峻轍，工業材料，**186** 期 82 (2002).

[20] 范元昌、蘇健忠、翁震灼、陳俊沐，工業材料，**186** 期 131 (2002).

[21] Q. D. Wang, W. D. Chen, X. Q. Zeng, Y.Z. Lu, W. J. Ding, Y. P. Zhu, X. P. Xu, M. Mabuchi, J. Mater. Sci. **36**, 3055 (2001).

[22] P. Li, B. Tang, E. G. Kandalova, Mater. Lett. **59**, 671 (2005).

[23] B. L. Mordike, Mater. Sci. Eng. **A324** ,103 (2002).

[24] 吳學陞. 工業材料 **149**, 154-165 (1999).

[25] K. L. Chopra. *Thin Film Phenomena*. McGraw-Hill, New York, USA. (1985).

[26] P. J. Hsieh. PhD Thesis, *Nanocrystallization and Amorphization of Zr Base Alloys*

during Accumulative Roll Bonding, National Sun Yat-Sen University, Kaohsiung, Taiwan, (2004).

[27] W. Buckel. Z. Phys. **138**, 136 (1954).

[28] E. J. Cotts, W. J. Meng and W. L. Johnson. Phys. Rev. Lett. **57**, 2295-2298 (1986).

[29] J. Dudonis, R. Brucas and A. Miniotas. Thin Solid Films **275**, 164-167 (1996).

[30] P. S. Grant. Prog. Mater. Sci. **39**, 497-545 (1995).

[31] B. Li, N. Nordstrom and E. J. Lavernia. Mater. Sci. Eng. A **237**, 207-215 (1997).

[32] R. S. Liu, J. Y. Li, K. J. Dong, C. X. Zheng and H. R. Liu. Mater. Sci. Eng. B **94**, 141-148 (2002).

[33] C. R. M. Afonso, C. Bolfarini, C. S. Kiminami, N. D. Bassim, M. J. Kaufman, M. F. Amateau, T. J. Eden and J. M. Galbraith. J. Non-Crystalline Solids **284**, 134-138 (2001).

[34] W. Klement, R. H. Willens and P. Duwez. Nature **187**, 869-870 (1960).

[35] M. S. El-Eskandarany and A. Inoue. Metall. Mater. Trans. A **33**, 135-143 (2002).

[36] C. C. Koch, O. B. Kavin, C. G. Mckamey and J. O. Scarbrough. Appl. Phys. Lett. **43**, 1017-1019 (1983).

[37] Y. Saito, H. Utsunomiya, N. Tsuji and T. Sakai. Acta Mater. **47**, 579-583 (1999).

[38] Z. P. Xing, S. B. Kang and H. W. Kim. Metall. Mater. Trans. A **33A**, 1521-1530 (2002).

[39] J. Lee, F. Zhou, K. H. Chung, N. J. Kim and E. J. Lavernia. Metall. Mater. Trans. A **32**, 3109-3115 (2001).

[40] A. Sagel, H. Sieber, H. J. Fecht and J. H. Perepezko. Acta Mater. **46**, 4233-4241 (1998).

[41] Z. P. Lu and C. T. Liu, Acta Mater. **50**, 3501-3512 (2002).

[42] D. E. Polk, Acta Metall. **20**, 485-& (1972).

[43] S. R. Nagel and J. Tauc, Phys. Rev. Lett. **35**, 380-383 (1975).

[44] H. S. Chen and B. K. Park, Acta Metall. **21**, 395-400 (1973).

[45] K. S. Dubey and P. Ramachandrarao, Int.l J. Rapid Solid. **5**, 127-135 (1990).

[46] S. H. Whang, Mater. Sci. and Eng. **57**, 87-95 (1983).

[47] T. Egami and Y. Waseda, J. of Non-Crystalline Solids **64**, 113-134 (1984).

[48] Z. P. Lu, Y. Liu, and C. T. Liu, *Evalution of glass-forming ability*. Bulk Metallic Glasses, ed. Michael K. Miller and P. K. Liaw., New York, Springer Science+Business Media. Chapter 4 (2008).

[49] G. J. Fan, H. Choo, and P. K. Liaw, J. of Non-Crystalline Solids **353**, 102-107 (2007).

[50] Q. J. Chen, J. Shen, D. L. Zhang, H. B. Fan, J. Sun, and D. G. McCartney, Materials Science and Engineering a-Structural Materials Properties Microstructure and Processing **433**, 155-160 (2006).

[51] Z. P. Lu and C. T. Liu, Phys. Rev. Lett. **91** (2003).

[52] X. H. Du, J. C. Huang, K. C. Hsieh, Y. H. Lai, H. M. Chen, J. S. C. Jang, and P. K. Liaw, Appl. Phys. Lett. **91** (2007).

[53] R. E. Reed-Hill, R. Abbaschian, *Physical Metallurgy Principles*, PWS, Boston, USA.

(1994).

[54] A. Inoue. Mater. Trans. JIM **36**, 866-875 (1995).

[55] A. Inoue, A. Takeuchi and T. Zhang. Metall. Mater. Trans. A **29**, 1779-1793 (1998).

[56] A. Inoue and K. Hashimoto. *Amorphous and Nanocrystalline Materials: Preparation, Properties, and Applications*, Springer-Verlag, Berlin and Heidelberg. (2001).

[57] A. Takeuchi and A. Inoue. Mater. Trans. **41**, 1372-1378 (2000).

[58] D. M. Mattox. *Handbook of Physical Vapor Deposition (PVD) Processing*, Noyes publications, New Jersey. (1998).

[59] K. Wasa, and S. Hayakawa, *Handbook of Sputter Deposition Technology*. (1992)

[60] A. Sagel, H. Sieber, H. J. Fecht and J. H. Perepezko. Acta Mater. **46**, 4233-4241 (1998).

[61] D. Turnbull. Contemp. Phys. **10**, 473-488 (1969).

[62] S. Veprek and M. Heintz. Plas. Chem. Plas. Proc. **10**, 3-26 (1990).

[63] S. Veprek and M. G. J. Veprek-Heijman. Appl. Phys. Lett. **56,** 1766-1768 (1990).

[64] Y. Liu, S. Hata, K. Wada and A. Shimokohbe. 14th IEEE International Conference on Micro Electro Mechanical Systems, 102-105 (2001).

[65] Y. P. Deng, Y. F. Guan, J. D. Fowlkes, S. Q. Wen, F. X. Liu, G. M. Pharr, P. K. Liaw, C. T. Liu, and P. D. Rack, Intermetall. **15** 1208-1216 (2007).

[66] F. Spaepen. Acta Matall. **25**, 407-415 (1977).

[67] A. S. Argon. Acta Matall. **27**, 47-58 (1979).

[68] L. H. Dai, M. Yan, L. F. Liu and Y. L. Bai. Appl. Phys. Lett. **87**, 141916 (2005).

[69] T. G. Park, S. Yi and D. H. Kim. Scripta Mater. **43**, 109-114 (2000).

[70] S. Pang, T. Zhang, K. Asami and A. Inoue. Mater. Trans. JIM **42**, 376-379 (2001).

[71] 張志溢，“以摩擦旋轉攪拌製程製作奈米細晶鎂基合金與複材之研發”，國立中山大學博士論文 (2008)

[72] B. Navinsek, P. Panjan, J. Krusic. Surf. Coat. Tech. **98**, 809-815 (1998).

[73] J. H. Ahn, D. Kwon. Mater. Sci. Eng. A **285**, 172-179 (2000).

[74] J. R. Tuck, A. M. Korsunsky, D. G. Bhat, S. J. Bull. Surf. Coat. Tech. **139**, 63-74 (2001).

[75] L. Qian, M. Li, Z. Zhou, H. Yang, X. Shi. Surf. Coat. Tech. **195**, 264-271(2005).

Table 1-1 The standard four-part ASTM designation system of alloy and temper for the magnesium alloy [3].

	First part	Second part	Third part	Fourth partt
Statement	Indicates the two principal alloying element	Indicates the amount of the two principal elements	Distinguishes between different alloys with the same percentage of the two principal alloying	Indicates condition (temper)
Method	Consists of two code letters representing the two main alloying elements arranged in order of decreasing percentage (or alphabetically if percentage are equal)	Consists of two numbers corresponding to rounded-off percentage of the two main alloying elements and arranged in same designation in first part	Consists of a letter of the alphabet assigned in order as compositions become standard	Consists of a letter followed by a number (separated from the third part of the designation by a hyphen)
Example	A-Al E-rare earth H-Th K-Zr M-Mn Q-Ag S-Si T-Sn W-Y Z-Zn	Whole numbers	Letters of alphabet except I and O	F-as fabricated O-annealed H10 and H11-strain hardened H23, H24 and H26-strain hardened and partially annealed T4-solutuon heat treatment T5-artificially aged only T6-solution heat treated and artificially aged

Table 1-2 The effect of separate solute addition on the mechanical properties [4].

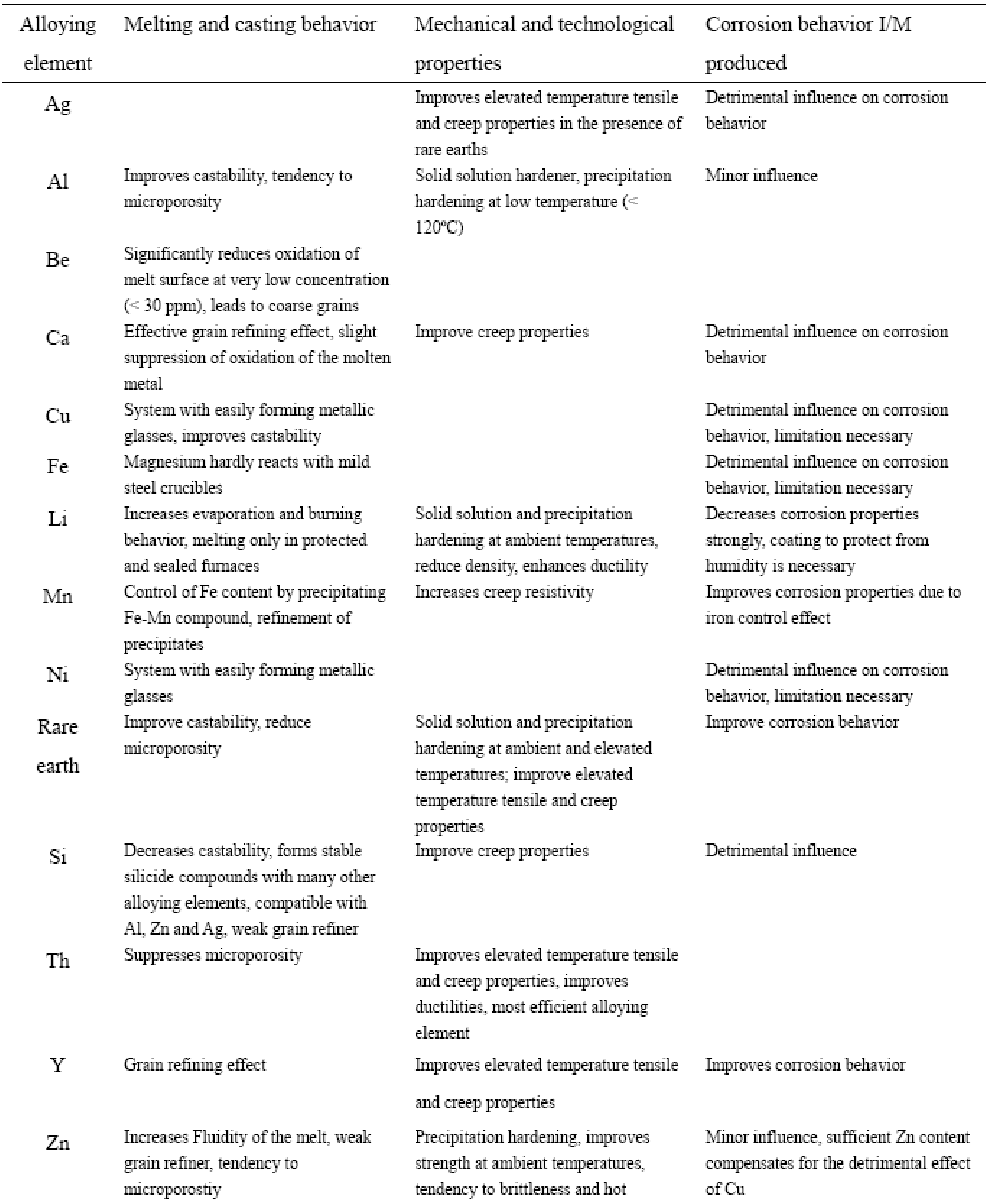

Alloying element	Melting and casting behavior	Mechanical and technological properties	Corrosion behavior I/M produced
Ag		Improves elevated temperature tensile and creep properties in the presence of rare earths	Detrimental influence on corrosion behavior
Al	Improves castability, tendency to microporosity	Solid solution hardener, precipitation hardening at low temperature (< 120°C)	Minor influence
Be	Significantly reduces oxidation of melt surface at very low concentration (< 30 ppm), leads to coarse grains		
Ca	Effective grain refining effect, slight suppression of oxidation of the molten metal	Improve creep properties	Detrimental influence on corrosion behavior
Cu	System with easily forming metallic glasses, improves castability		Detrimental influence on corrosion behavior, limitation necessary
Fe	Magnesium hardly reacts with mild steel crucibles		Detrimental influence on corrosion behavior, limitation necessary
Li	Increases evaporation and burning behavior, melting only in protected and sealed furnaces	Solid solution and precipitation hardening at ambient temperatures, reduce density, enhances ductility	Decreases corrosion properties strongly, coating to protect from humidity is necessary
Mn	Control of Fe content by precipitating Fe-Mn compound, refinement of precipitates	Increases creep resistivity	Improves corrosion properties due to iron control effect
Ni	System with easily forming metallic glasses		Detrimental influence on corrosion behavior, limitation necessary
Rare earth	Improve castability, reduce microporosity	Solid solution and precipitation hardening at ambient and elevated temperatures; improve elevated temperature tensile and creep properties	Improve corrosion behavior
Si	Decreases castability, forms stable silicide compounds with many other alloying elements, compatible with Al, Zn and Ag, weak grain refiner	Improve creep properties	Detrimental influence
Th	Suppresses microporosity	Improves elevated temperature tensile and creep properties, improves ductilities, most efficient alloying element	
Y	Grain refining effect	Improves elevated temperature tensile and creep properties	Improves corrosion behavior
Zn	Increases Fluidity of the melt, weak grain refiner, tendency to microporostiy	Precipitation hardening, improves strength at ambient temperatures, tendency to brittleness and hot	Minor influence, sufficient Zn content compensates for the detrimental effect of Cu

Table 1-3 Fundamental properties and application fields of bulk amorphous and nanocrystalline alloys [7].

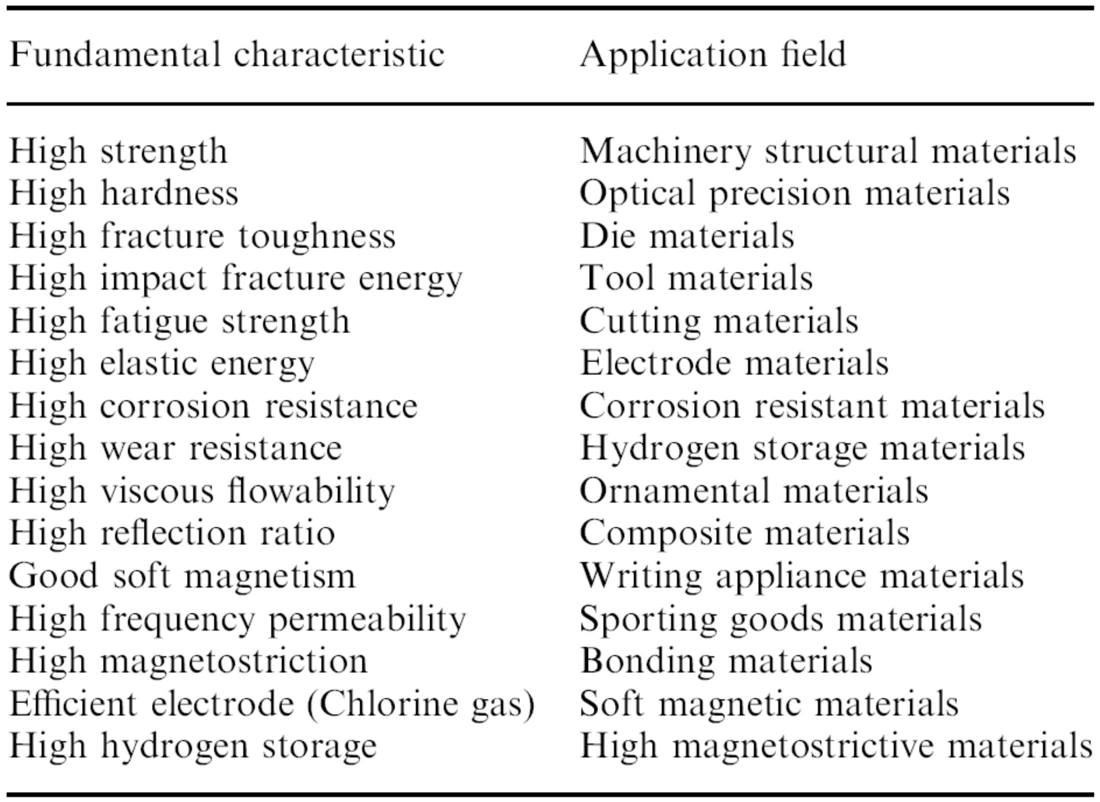

Fundamental characteristic	Application field
High strength	Machinery structural materials
High hardness	Optical precision materials
High fracture toughness	Die materials
High impact fracture energy	Tool materials
High fatigue strength	Cutting materials
High elastic energy	Electrode materials
High corrosion resistance	Corrosion resistant materials
High wear resistance	Hydrogen storage materials
High viscous flowability	Ornamental materials
High reflection ratio	Composite materials
Good soft magnetism	Writing appliance materials
High frequency permeability	Sporting goods materials
High magnetostriction	Bonding materials
Efficient electrode (Chlorine gas)	Soft magnetic materials
High hydrogen storage	High magnetostrictive materials

Table 2-1 Binary amorphous systems and mixing enthalpy values calculated based on Miedema's macroscopic model [57].

	Mg	**Cu**	**Y**	**Gd**	**Ag**	**B**
Mg		**-3**	**-6**		**-10**	
Cu	**-3**		**-22**	**-22**	**2**	**0**
Y	**-6**	**-22**			**-29**	**-50**
Gd		**-22**				**-50**
Ag	**-10**	**2**	**-29**			
B		**0**	**-50**	**-50**		

Table 3-1 Chemical composition of the AZ31 Mg alloy (in wt%).

Material	Mg	Al	Zn	Mn	Si	Fe	Cu	Ni
AZ31	Bal.	3.02	1.01	0.30	0.0067	0.0028	0.0031	0.0001

Table 4-1 Composition difference between the alloy targets and the as-deposited thin films. The compositions of the film are analyzed by SEM/EDS.

Sample	Atomic composition	
Pd-Cu-Si Target	$Pd_{77.5}Cu_6Si_{16.5}$	
	Individual	Average
As-deposited thin film	$Pd_{79}Cu_4Si_{17}$ $Pd_{78}Cu_8Si_{14}$ $Pd_{77}Cu_5Si_{18}$ $Pd_{75}Cu_6Si_{19}$ $Pd_{77}Cu_8Si_{15}$	$Pd_{77}Cu_6Si_{17}$

Table 4-2 The fitting parameters of the PCS TFMGs deposited on the AZ31 substrate obtained from the nanoindentation data.

Thickness (nm)	H_s (GPa)	H_f (GPa)	k	X
30	0.97±0.10	4.92±0.55	3.34	1.35
50	1.11±0.07	5.53±0.39	5.85	1.52
100	1.14±0.01	5.92±0.21	6.58	1.72
200	1.20±0.05	6.59±0.14	7.08	1.76
300	0.97±0.03	6.72±0.17	10.72	1.85
500	0.85±0.04	6.98±0.18	11.34	1.90
1000	0.70±0.02	7.38±0.26	14.36	1.92
2000	0.69±0.04	7.98±0.31	22.03	2.26

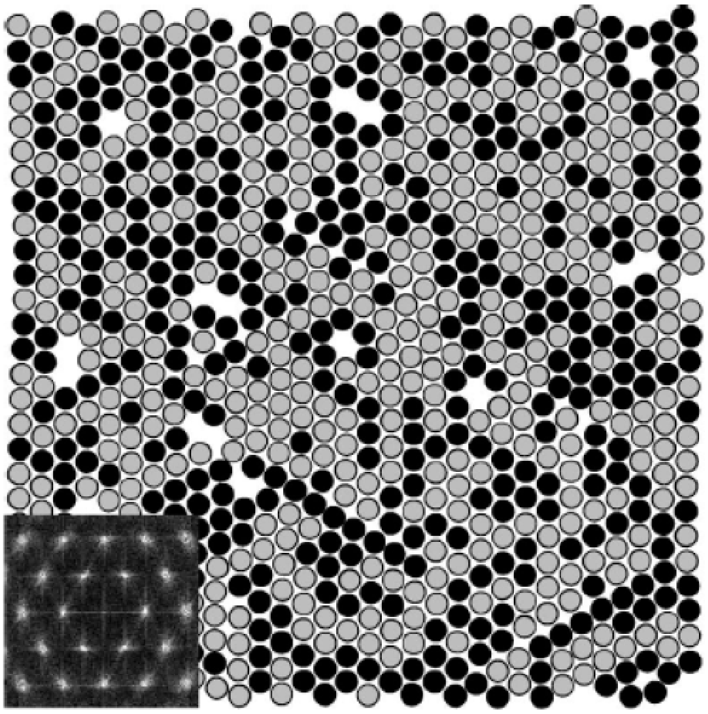

Figure 1-1 The atomic arrangment of long-range-order structure [5].

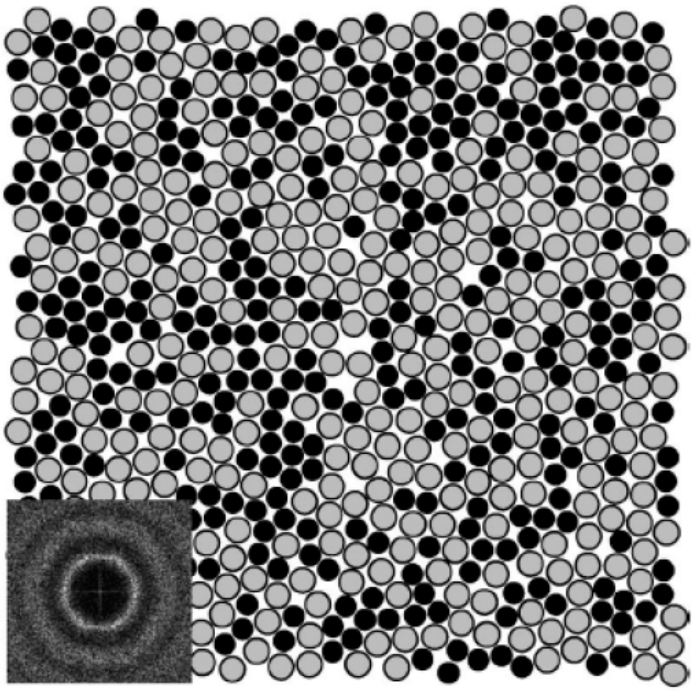

Figure 1-2 The atomic arrangment of short-range-order structure [5].

Figure 1-3 The shiny and smooth apperance of metallic glasses [6].

Figure 1-4 The frame for the upscale models of the Vertu mobile phone is made of liquid-metal alloy due to its high strength, hardness, and scratch resistance [9].

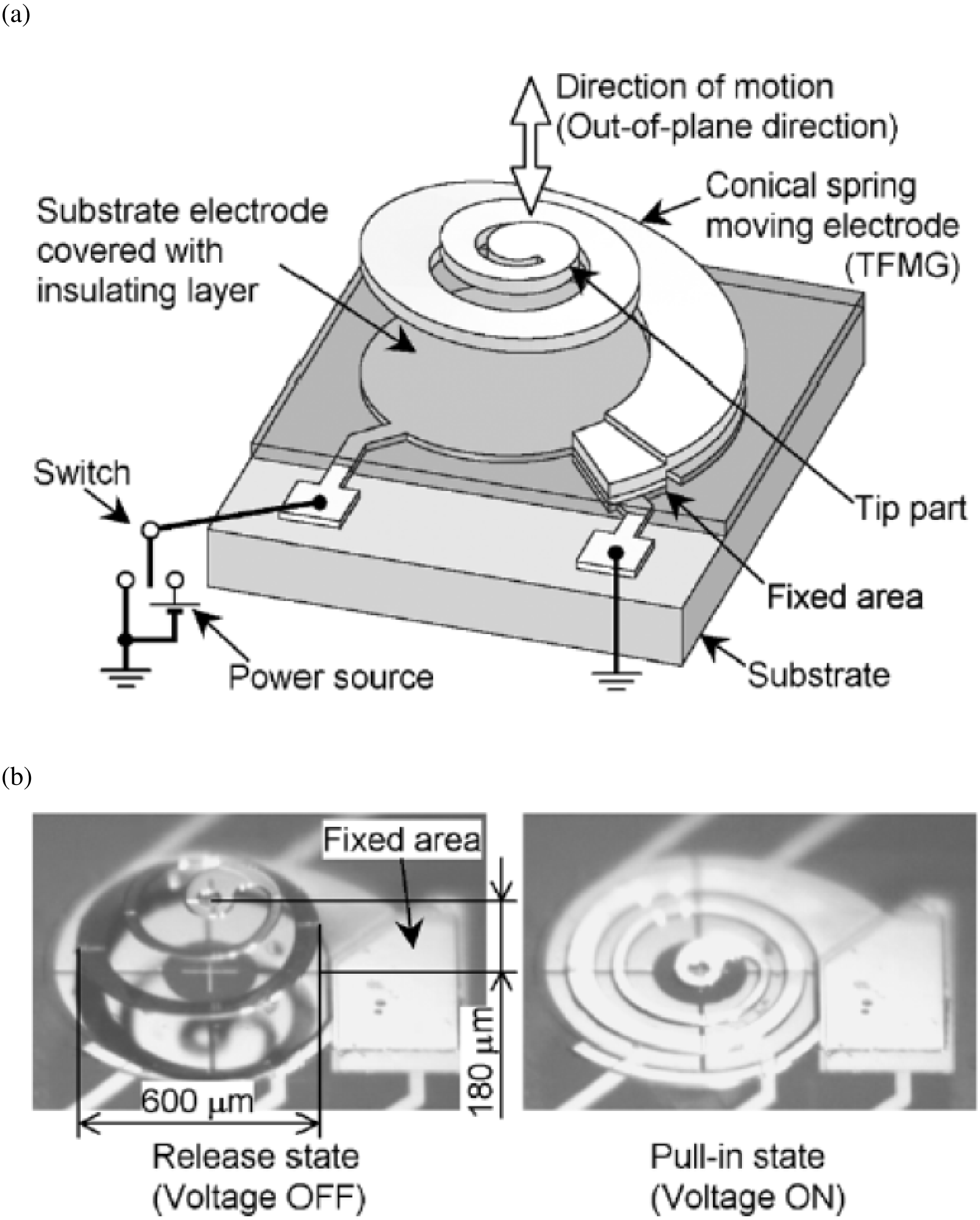

Figure 1-5 (a) Conical spring of microactuator, and (b) a fundamental structure of micro-switch made of thin film metallic glasses [10].

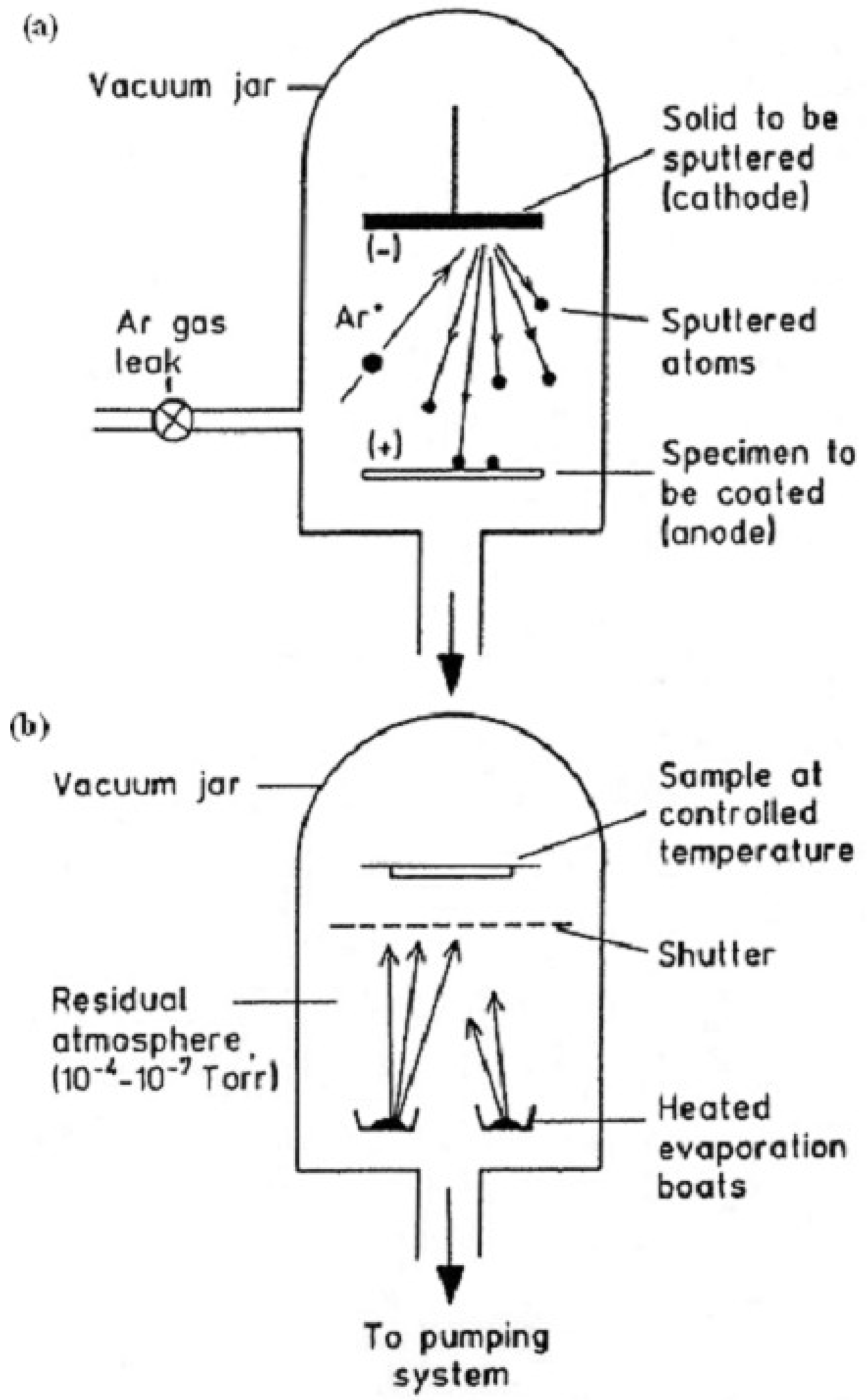

Figure 2-1 Schematic drawing of (a) sputtering and (b) vacuum evaporation [26].

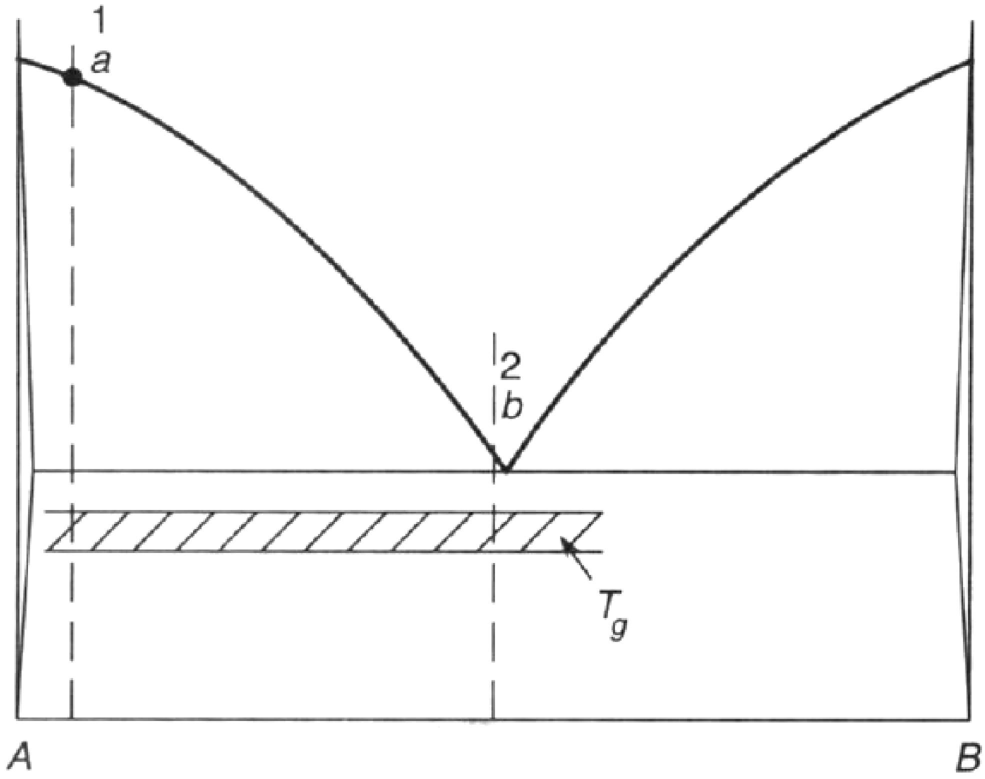

Figure 2-2 Schematic drawing of binary phase diagram [53].

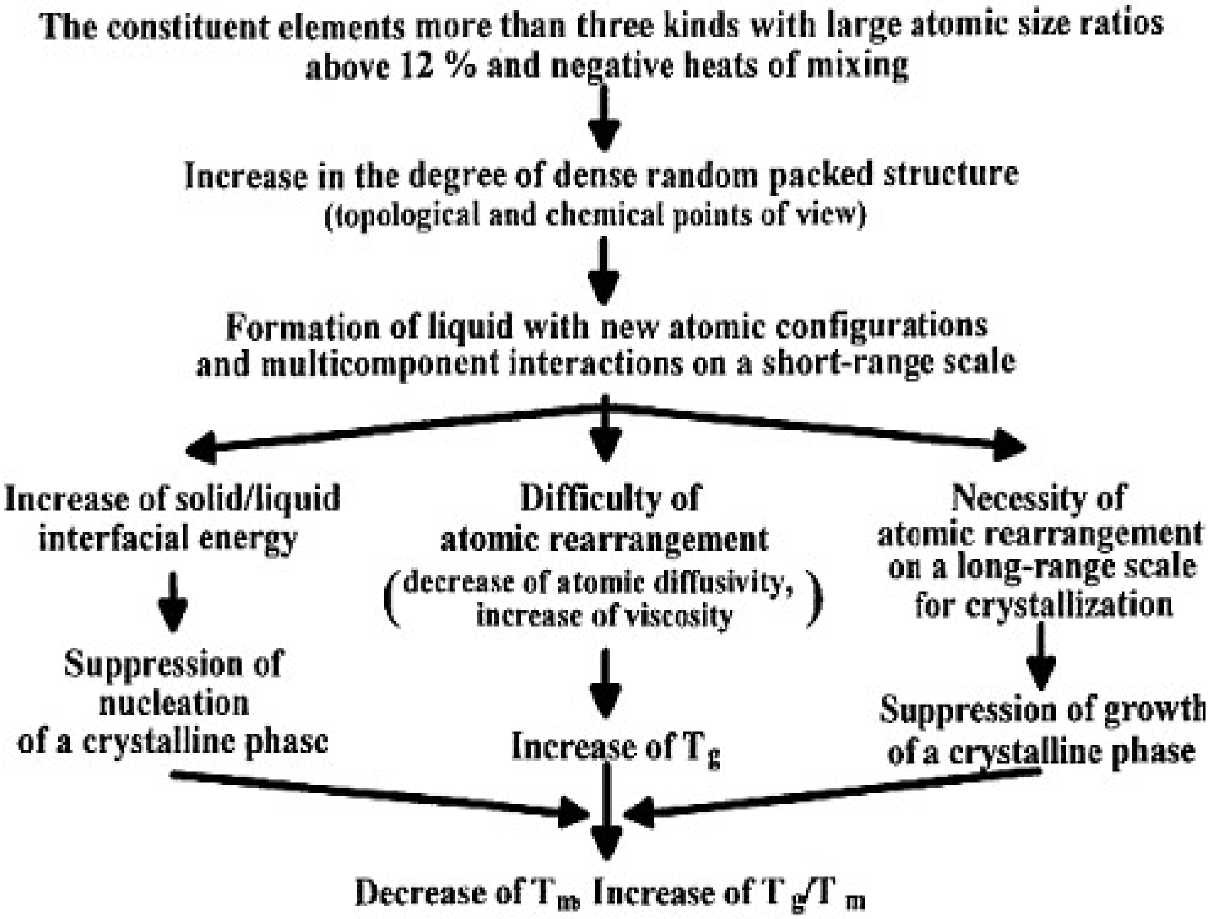

Figure 2-3 Mechanisms for the stabilization of supercooled liquid and the high glass-forming ability [7].

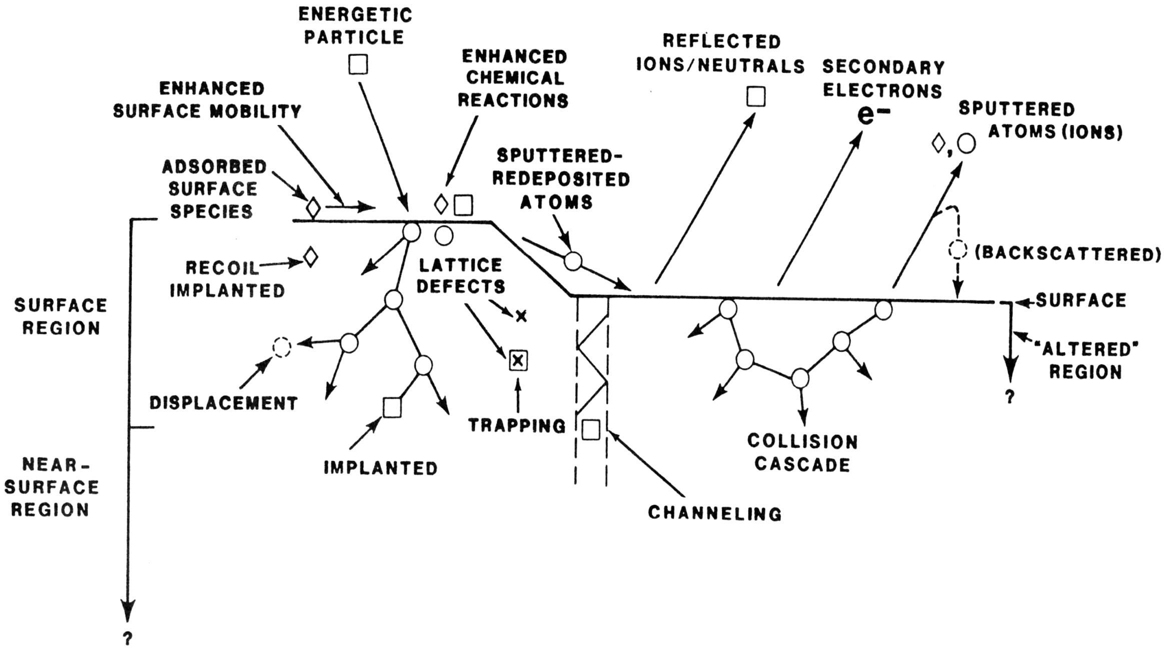

Figure 2-4 Events that occur on a surface being bombarded with energetic atomic-sized particles [58].

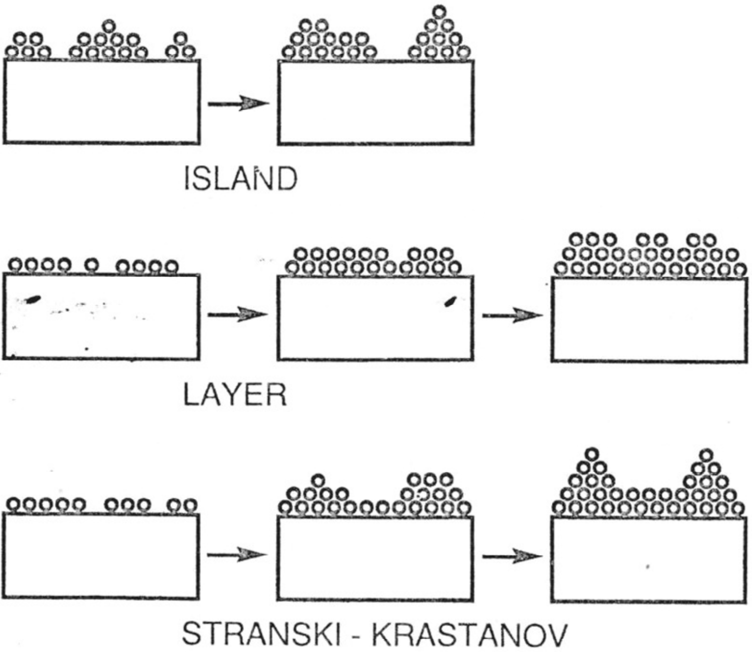

Figure 2-5 Schematic illustrations of three basic growth modes for thin film [61].

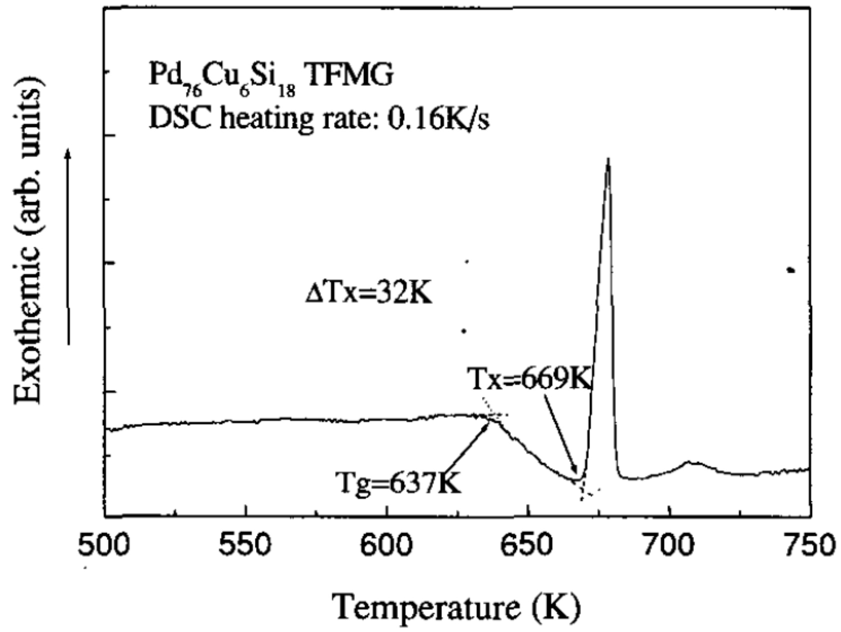

Figure 2-6 DSC thermography curve of the Pd-TFMG [15].

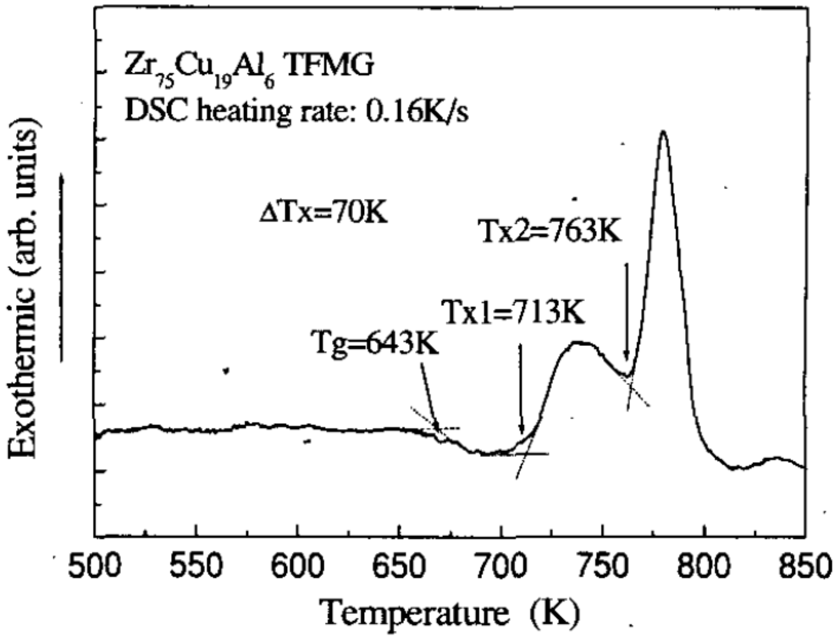

Figure 2-7 DSC thermography curve of the Zr-TFMG [64].

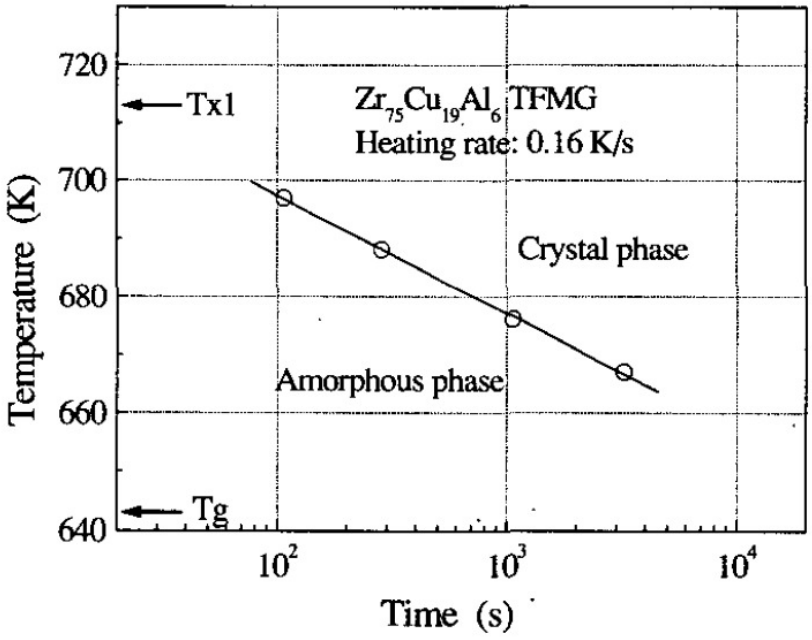

Figure 2-8 TTT diagram for the onset of crystallization in the Zr-TFMG [64].

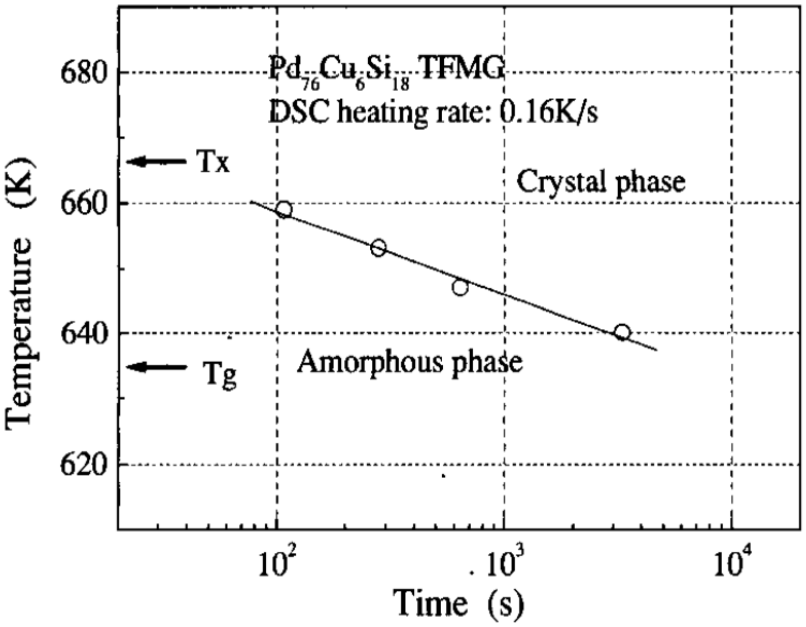

Figure 2-9 TTT diagram for the onset of crystallization in the Pd-TFMG [64].

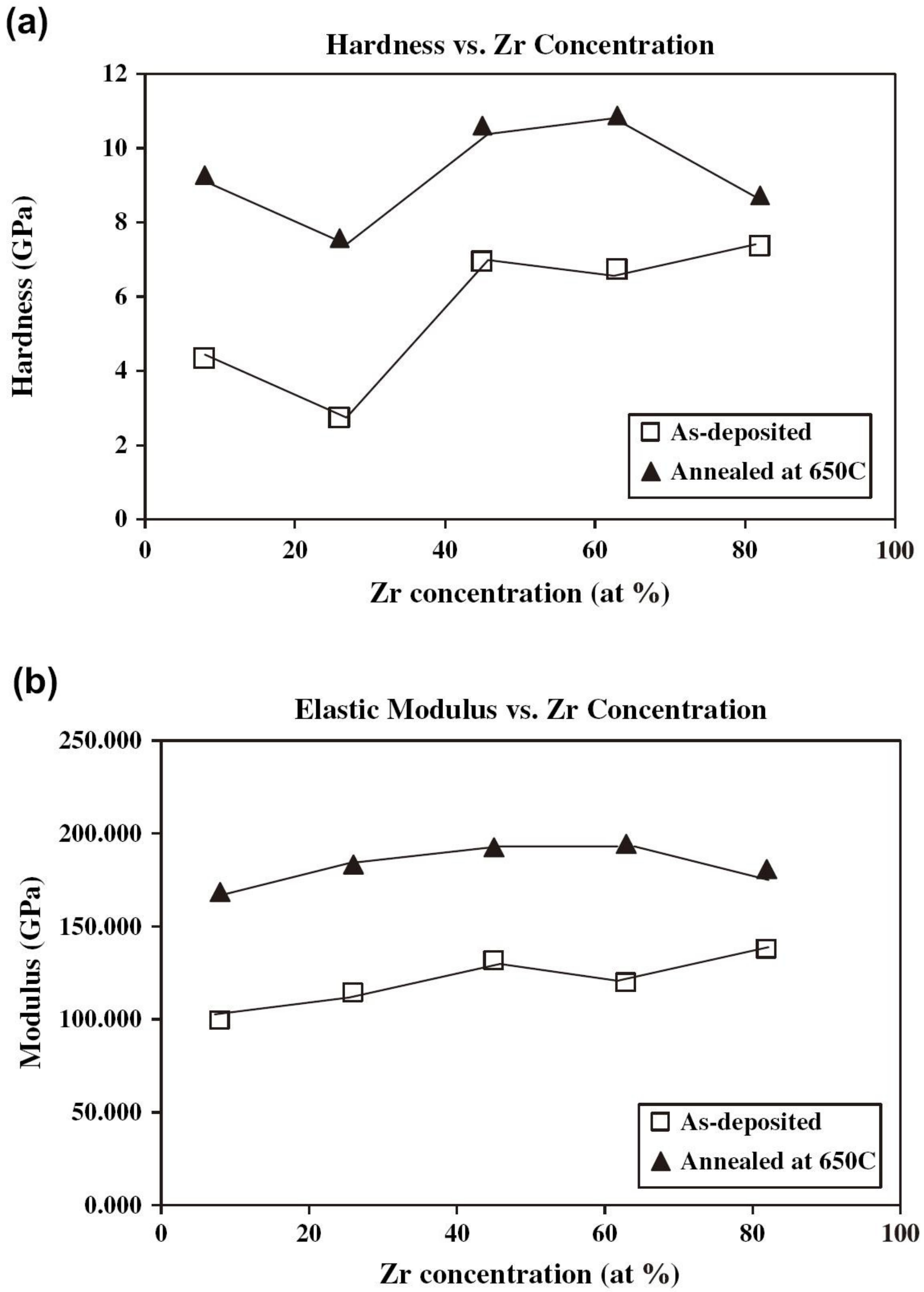

Figure 2-10 (a) Nanoindentation hardness measurement results of the as-deposited and the annealed films as a function of the concentration of Zr-Cu-Al TFMGs; (b) Nanoindentation Young's modulus measurement results of the as-deposited and the annealed films as a function of the concentration of Zr-based TFMGs [65].

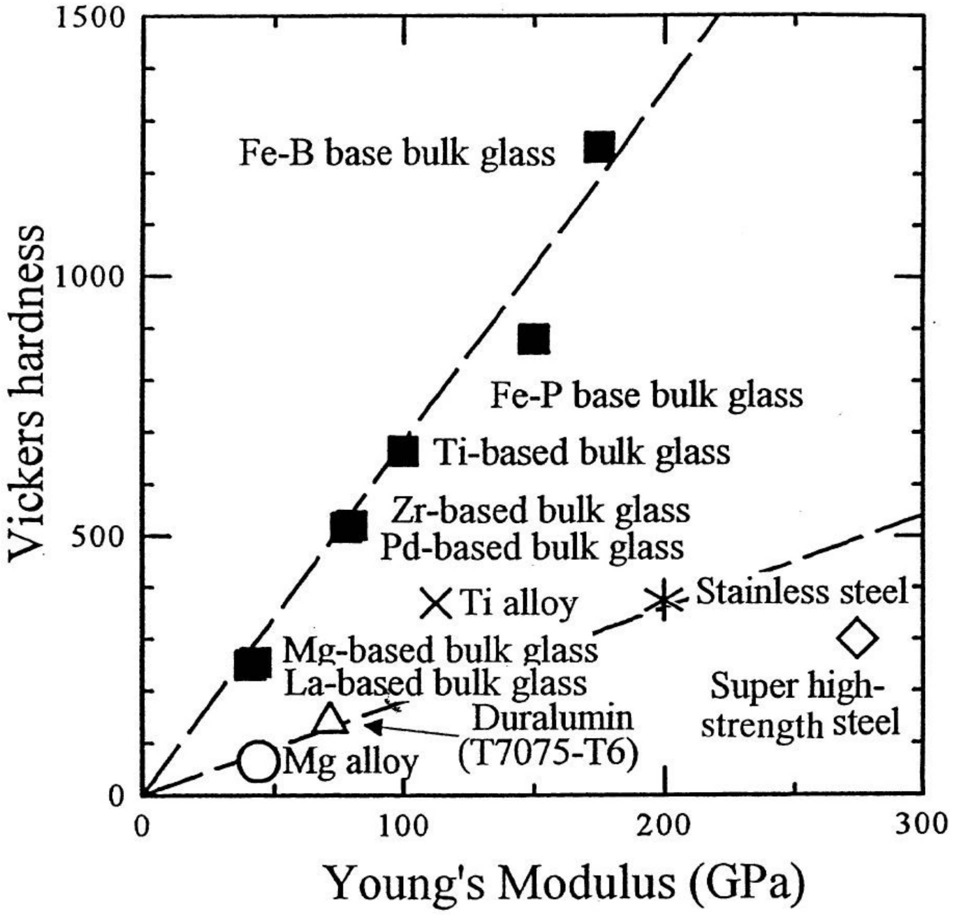

Figure 2-11 Relationship between Vickers hardness (H_v) and Young's modulus (GPa) for various BMGs [7].

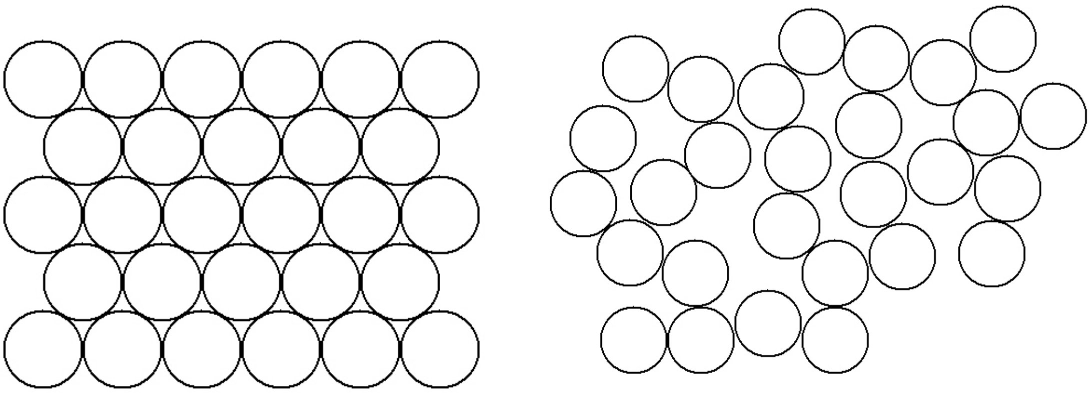

Figure 2-12 The arrangement of atoms in (a) crystalline and (b) amorphous states.

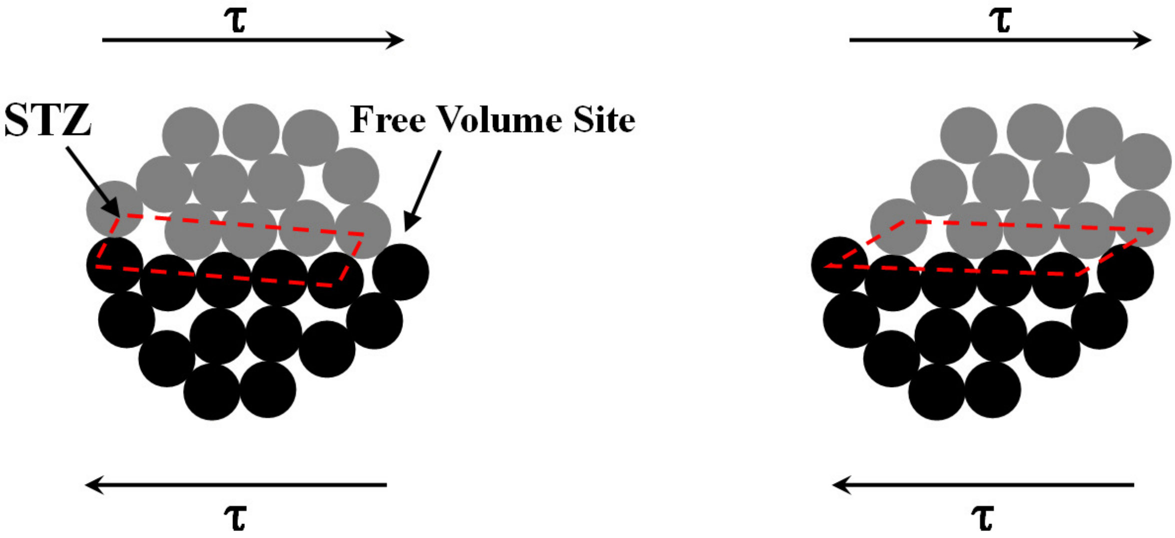

Figure 2-13 The illustration of the shear transformation zones (STZs) (a) before shear deformation and (b) after shear deformation in two-dimensional space.

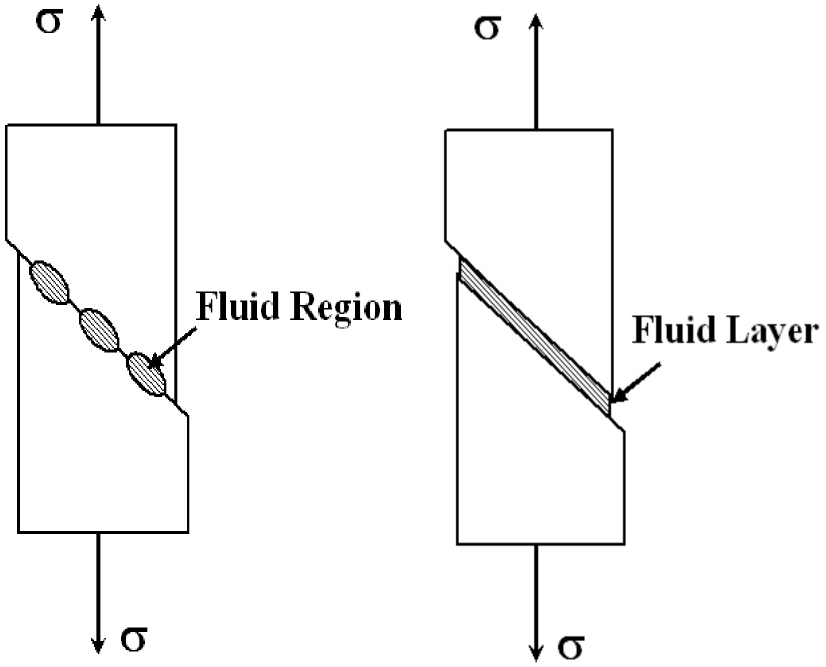

Figure 2-14 Schematic drawing of the fluid zones of amorphous alloy.

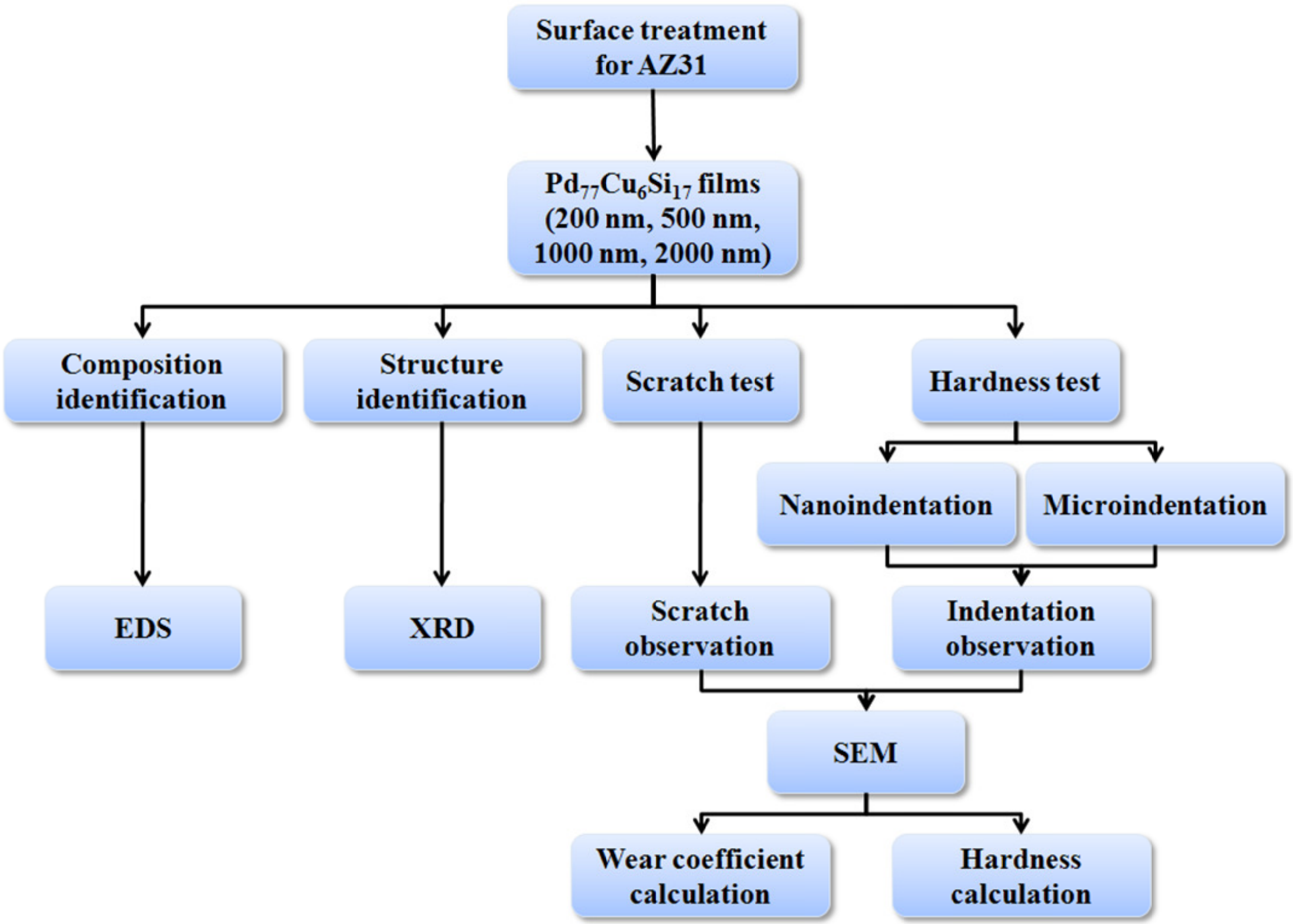

Figure 3-1 The flow chart of the experimental procedures in this study.

Figure 3-2 The standard Nano Indenter® XP is a complete, turnkey system consisting of the major components illustrated.

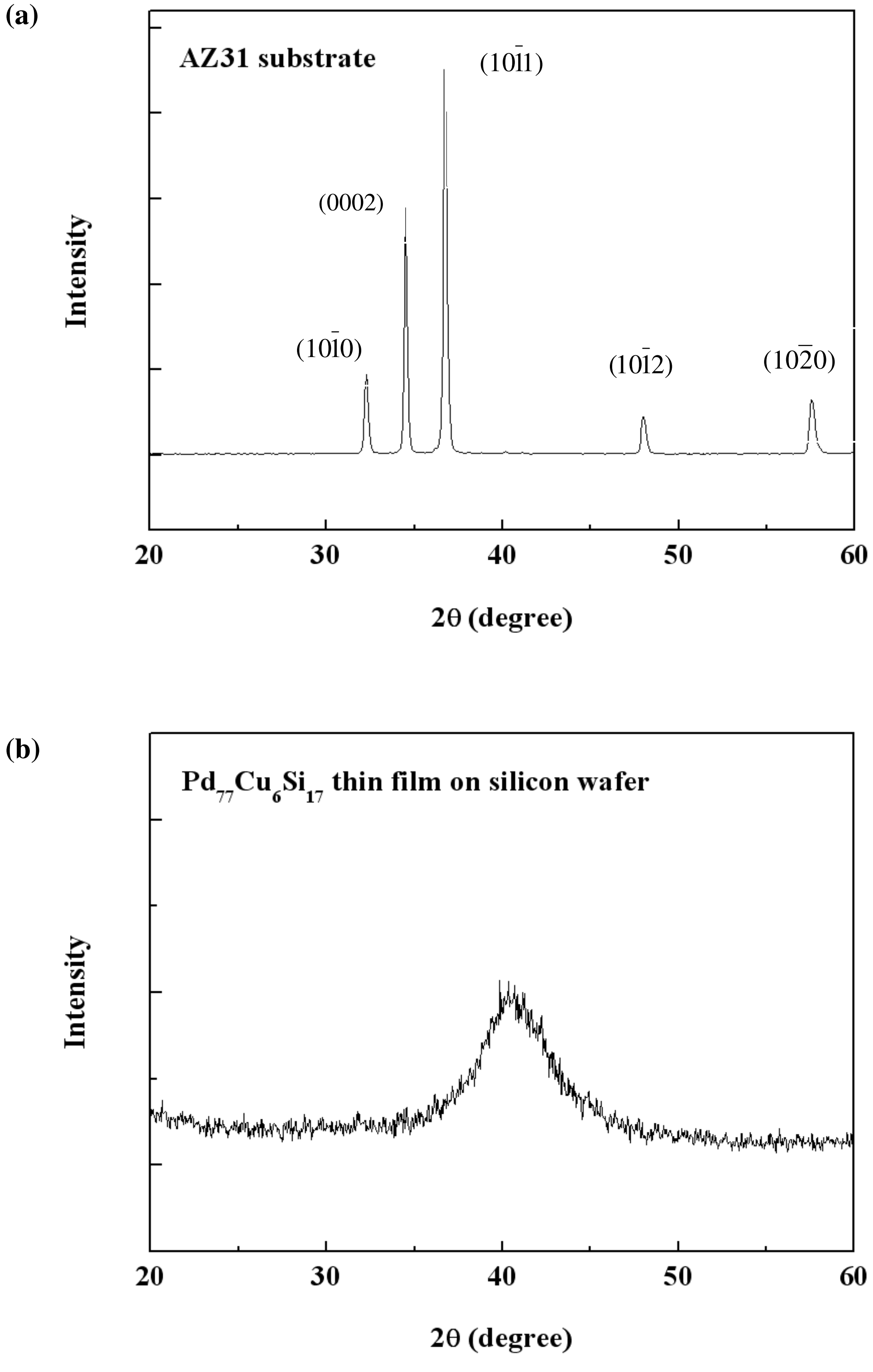

Figure 4-1 XRD pattern of (a) the AZ31 substrate, (b) the $Pd_{77}Cu_6Si_{17}$ thin film deposited on silicon substrate.

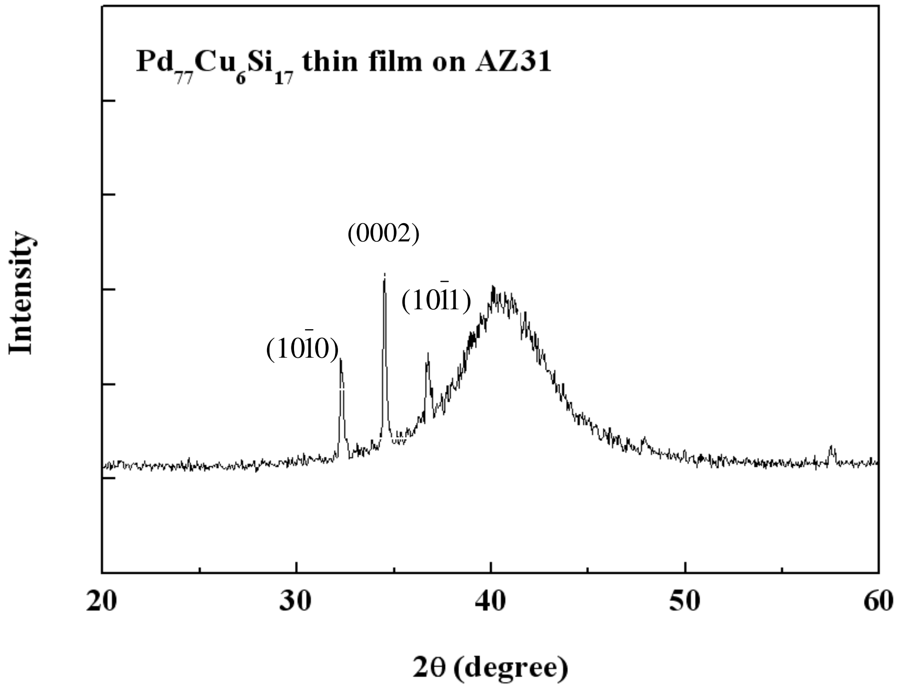

Figure 4-2 XRD pattern of the $Pd_{77}Cu_6Si_{17}$ thin film deposited on the AZ31 substrate.

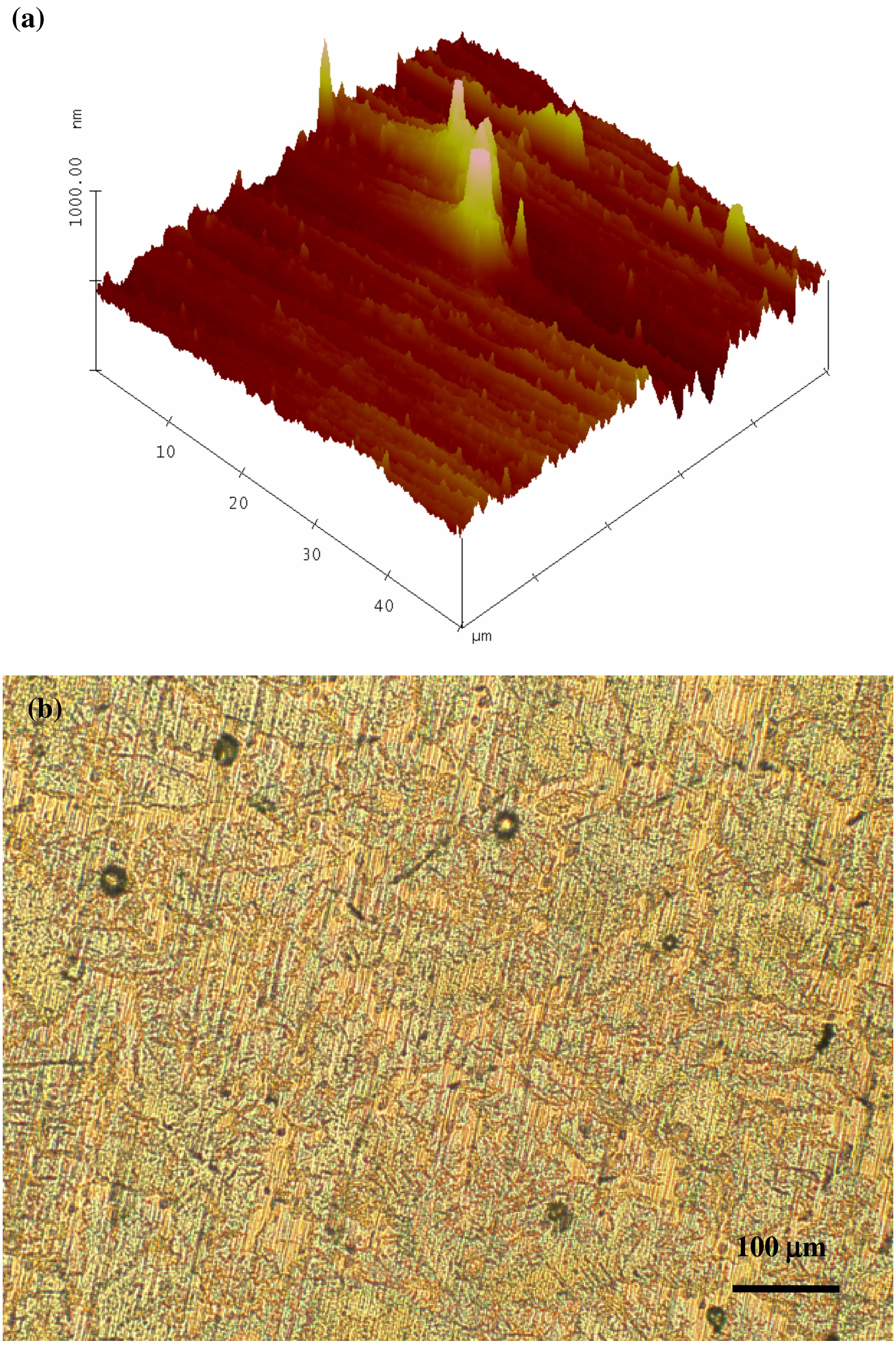

Figure 4-3 (a) AFM image of the AZ31 substrate topography, and the roughness Ra is ~70 nm after diamond paste polishing, (b) OM image of the AZ31 substrate mophology.

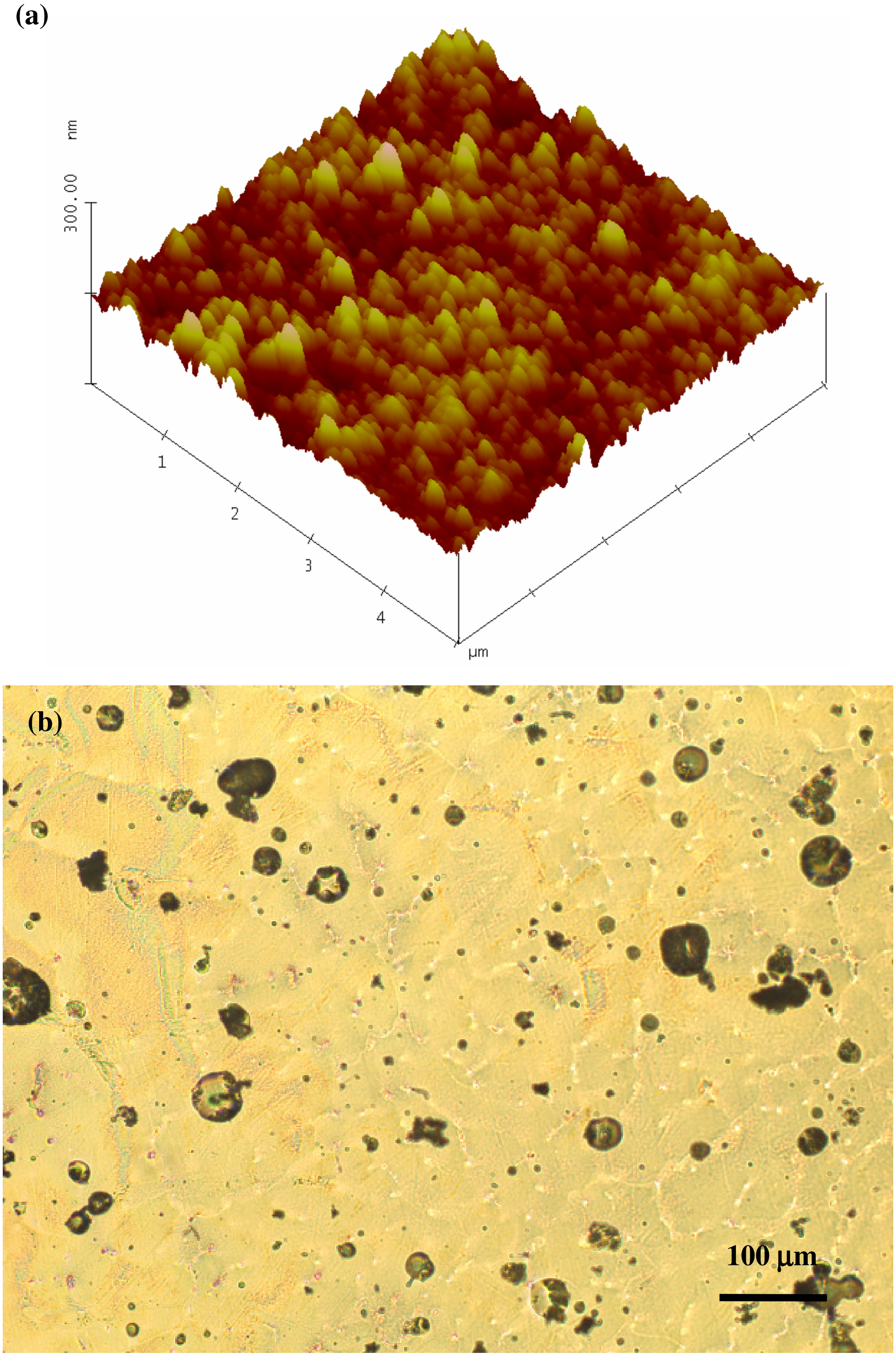

Figure 4-4 (a) AFM image of the AZ31 substrate topography, and the roughness Ra is ~10 nm after SiO_2 polishing, (b) OM image of the AZ31 substrate morphology.

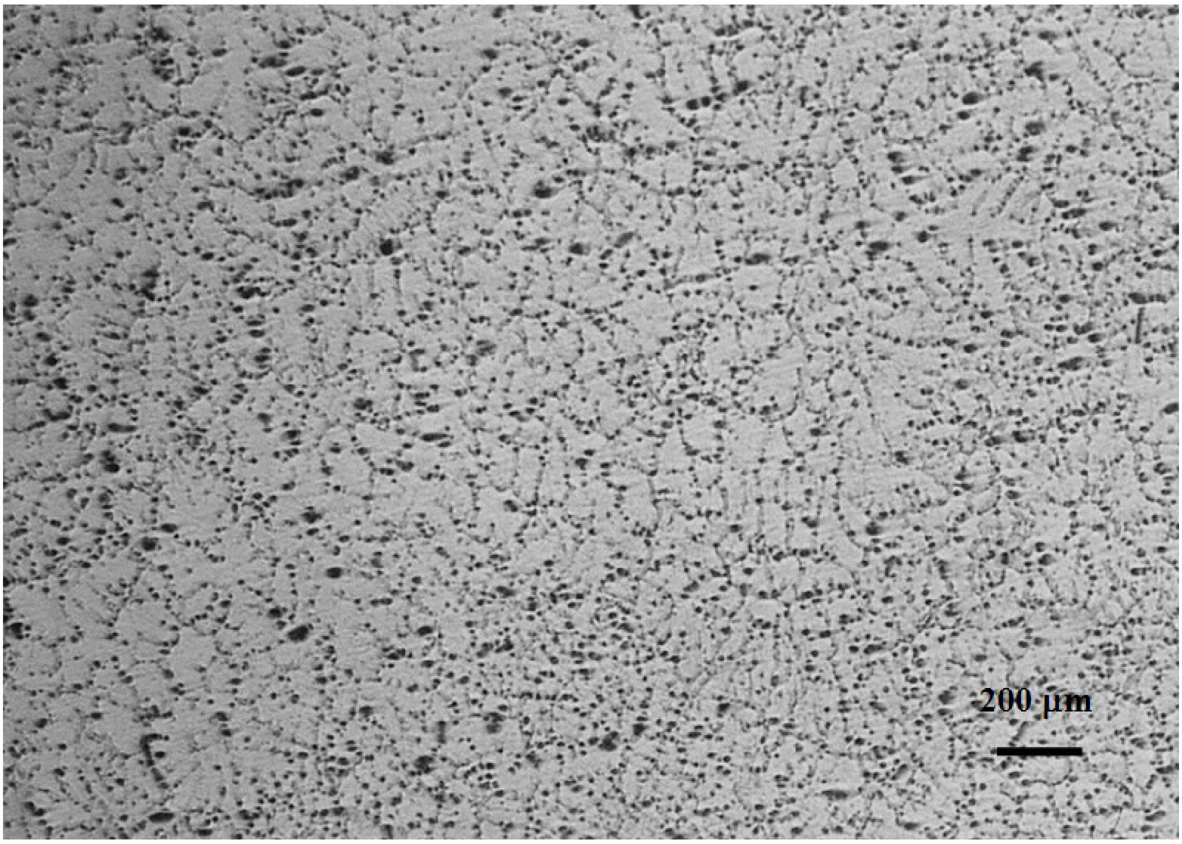

Figure 4-5 The microstructure of the as-received AZ31 billet after etching.

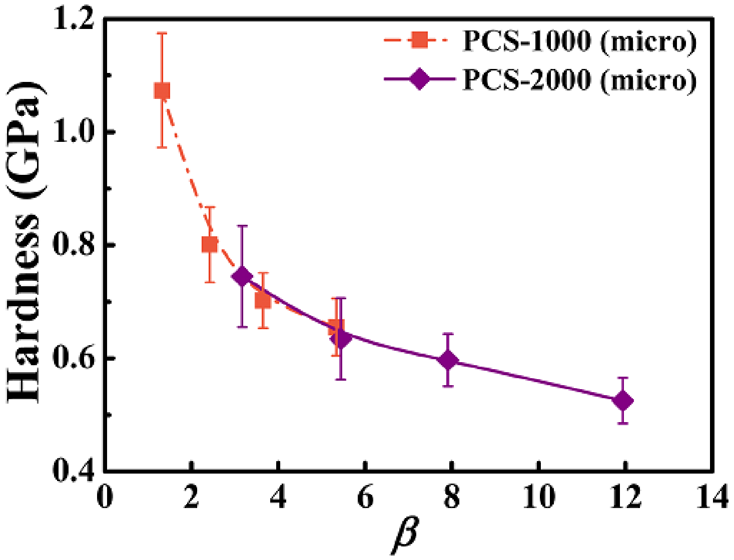

Figure 4-6 The hardness-β curves of the PCS-1000 and PCS-2000, measured from the microhardness tests.

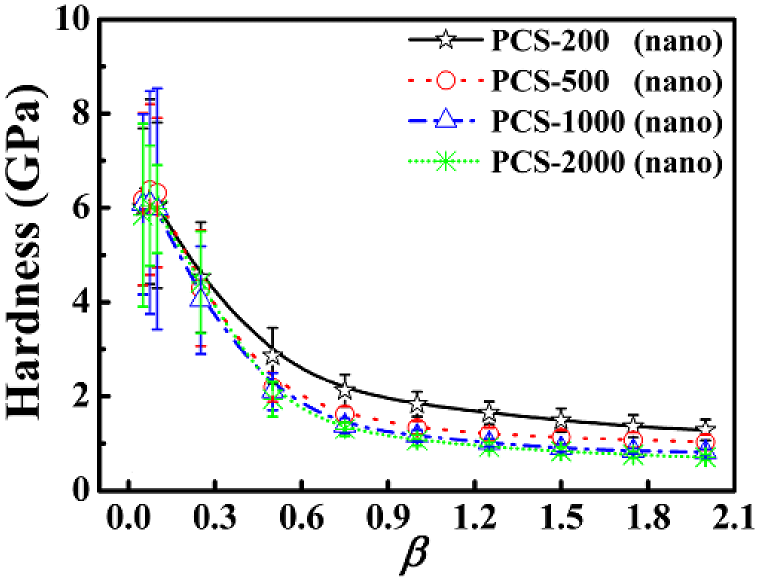

Figure 4-7 The hardness-β curves of the PCS-200, PCS-500, PS-1000, and PCS-2000, measured by nanoindentaiton tests.

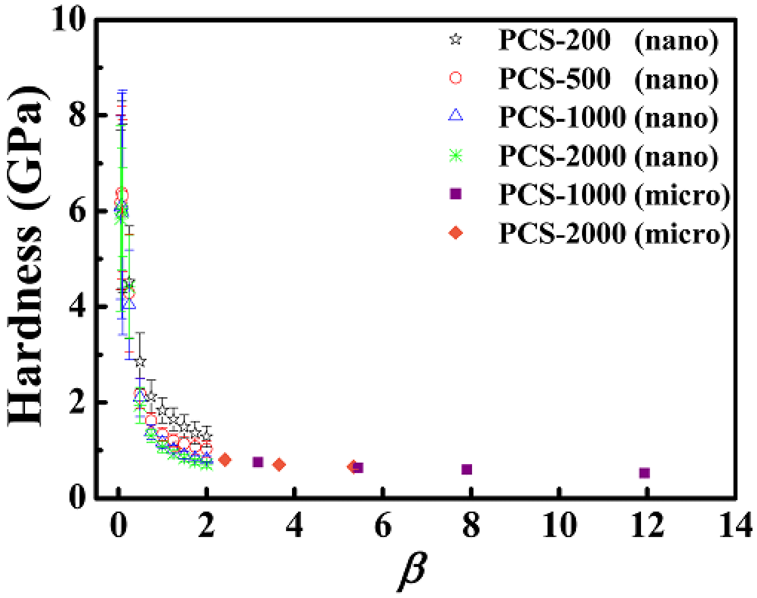

Figure 4-8 The combined hardness-β plots for all the experimental data measured from the microhardness and nanoindentaiton tests.

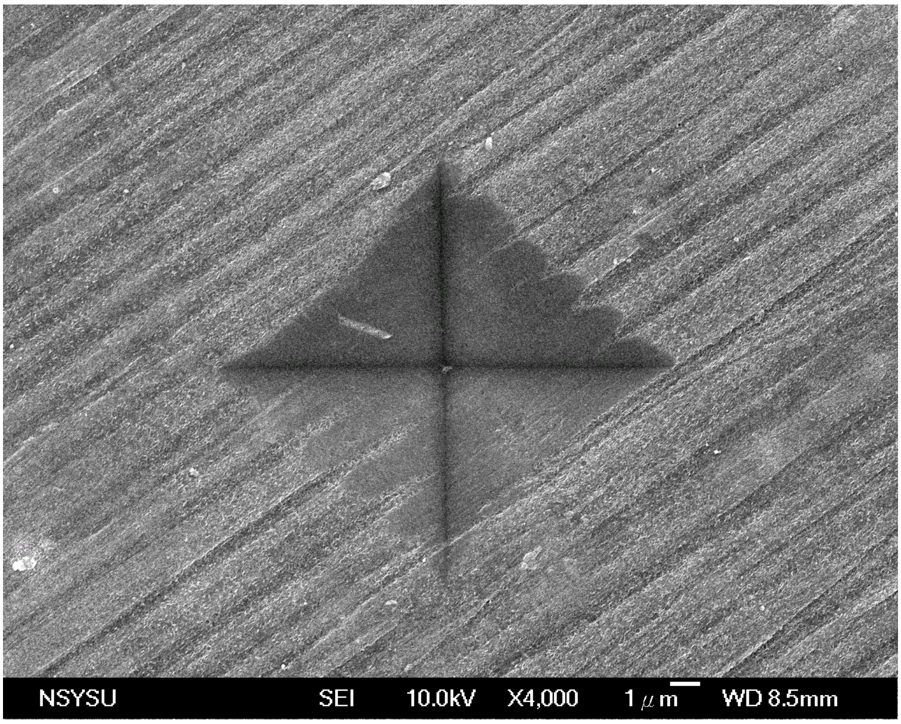

Figure 4-9 The SEI image of the AZ31 substrate at an applied load of 10 g.

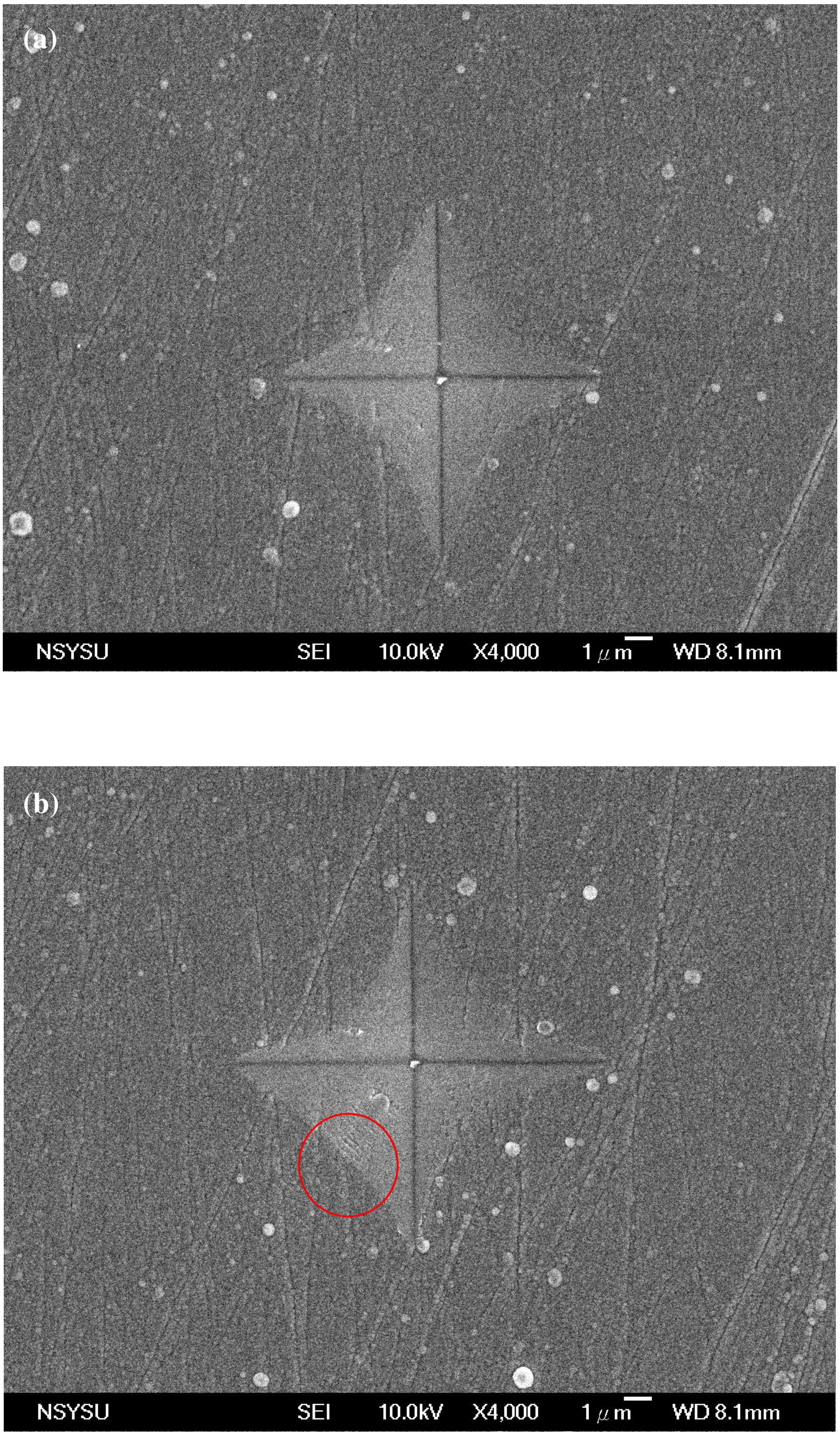

Figure 4-10 The SEI image of the $Pd_{77}Cu_6Si_{17}$ TFMG 2000 nm in thickness (a) without obvious shear bands, and (b) with shear bands at an applied load of 10 g.

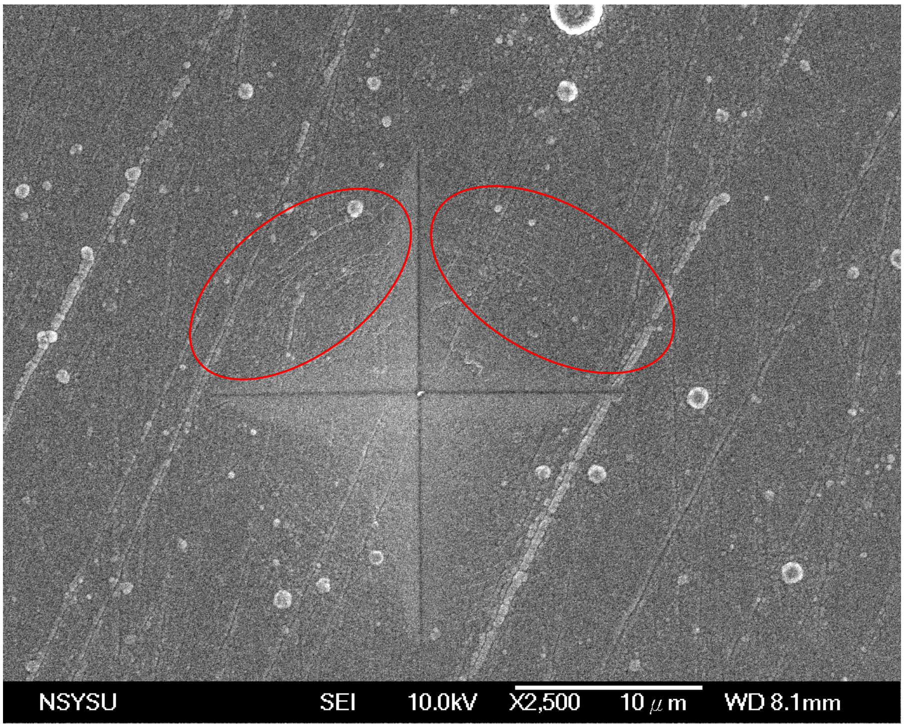

Figure 4-11 The SEI image of the $Pd_{77}Cu_6Si_{17}$ TFMG 2000 nm in thickness at an applied load of 25 g.

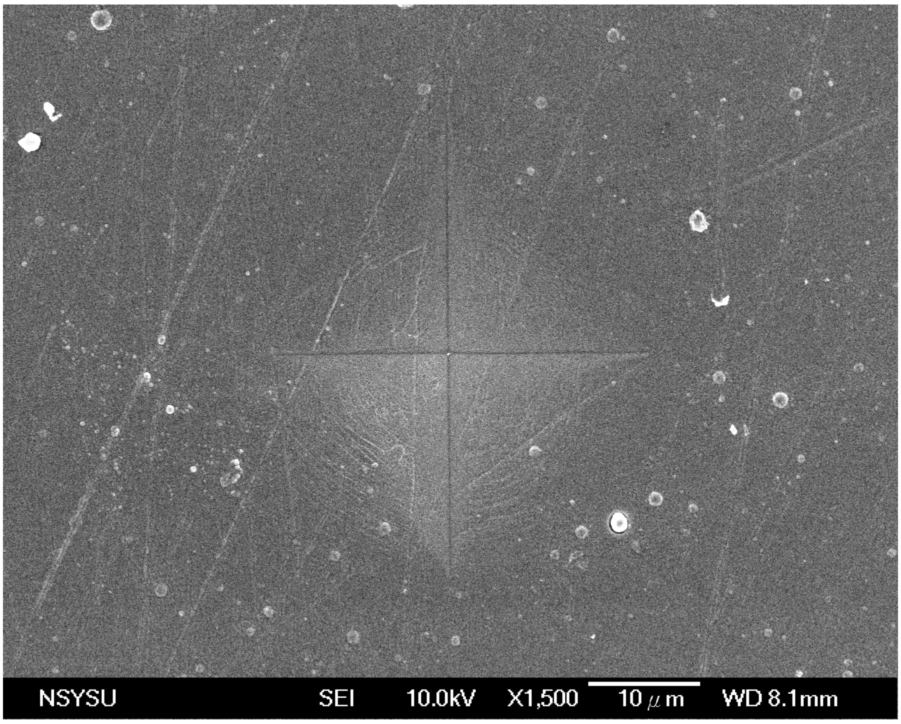

Figure 4-12 The SEI image of the $Pd_{77}Cu_6Si_{17}$ TFMG 2000 nm in thickness at an applied load of 50 g.

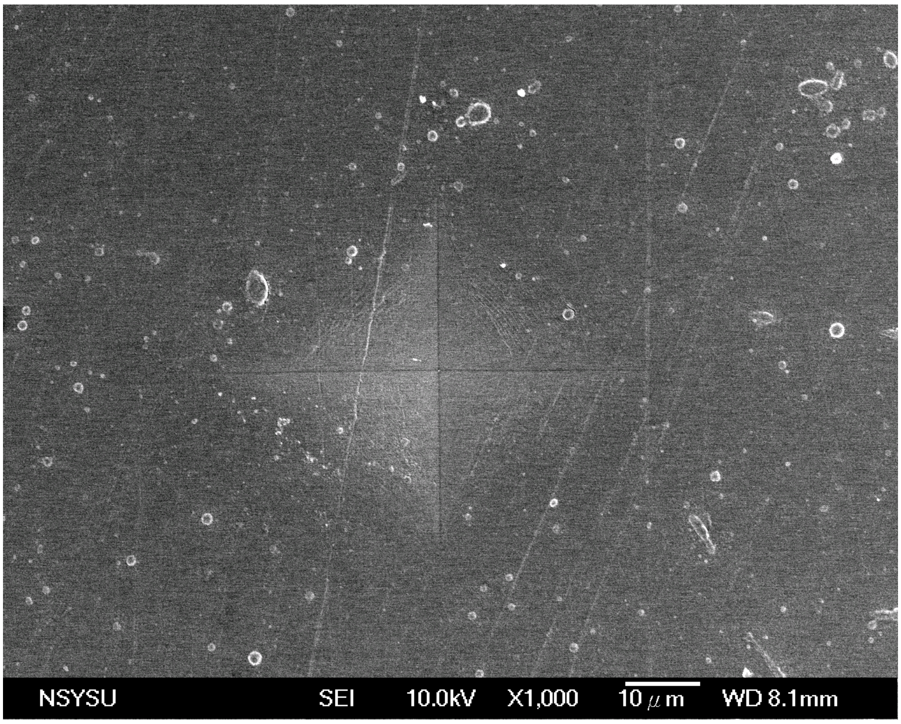

Figure 4-13 The SEI image of the $Pd_{77}Cu_6Si_{17}$ TFMG 2000 nm in thickness at an applied load of 100 g.

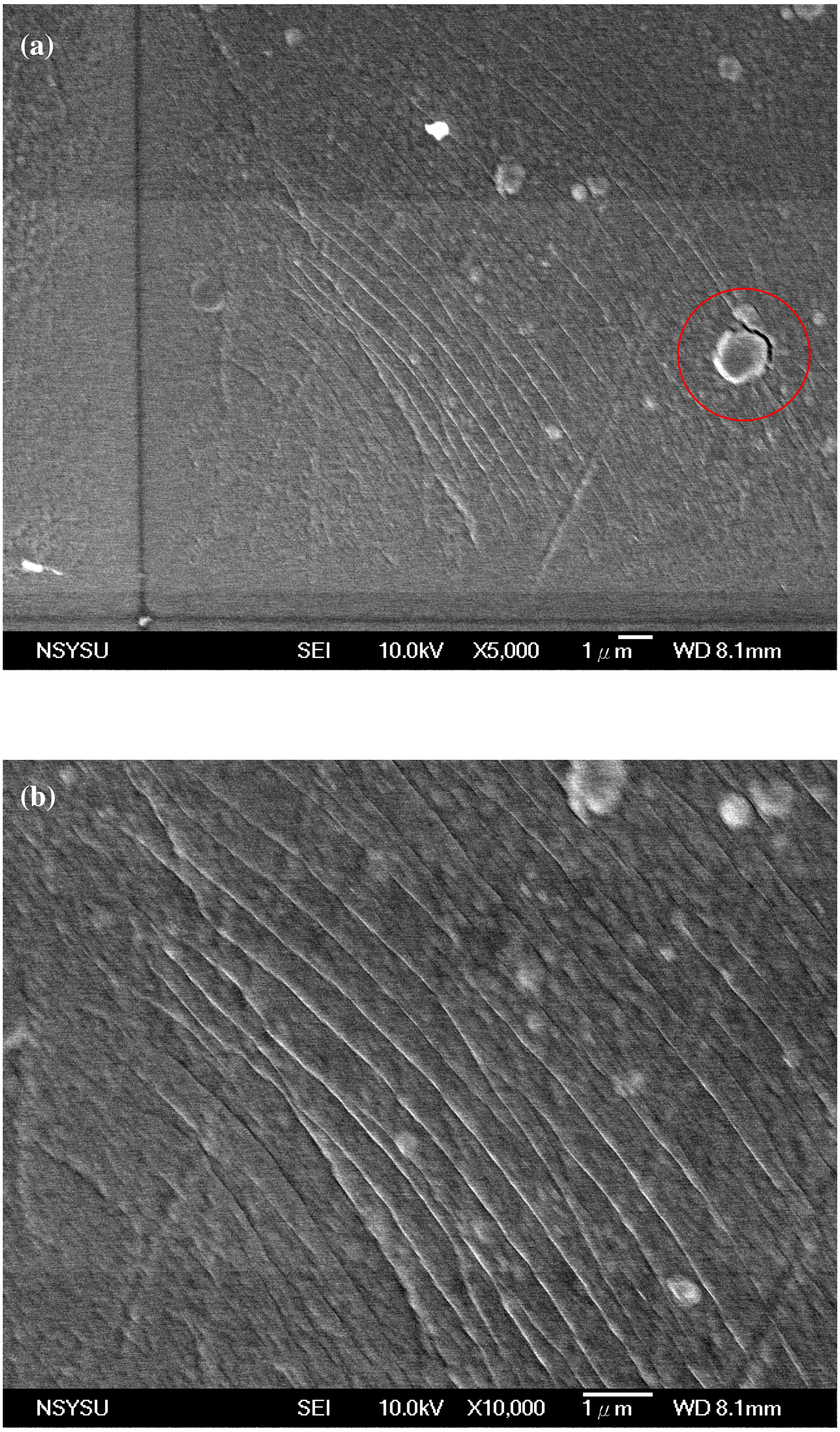

Figure 4-14 (a) The enlarged SEI image taken from Figure 4-13, (b) the enlarged SEI image taken from Figure 4-14 (a).

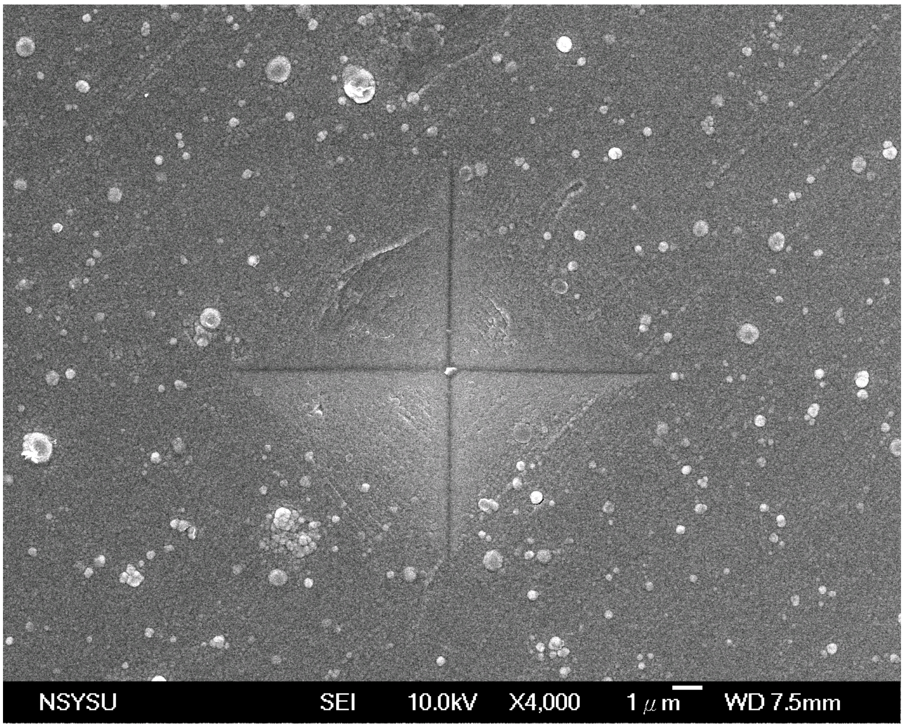

Figure 4-15 The SEI image of the $Pd_{77}Cu_6Si_{17}$ TFMG 1000 nm in thickness at an applied load of 10 g.

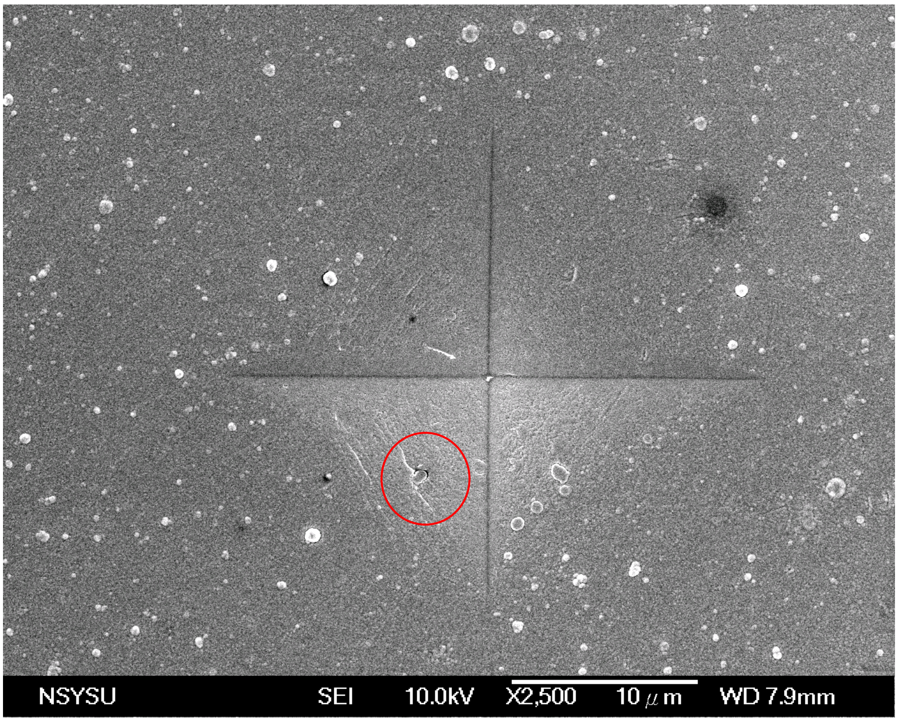

Figure 4-16 The SEI image of the $Pd_{77}Cu_6Si_{17}$ TFMG 1000 nm in thickness at an applied load of 25 g.

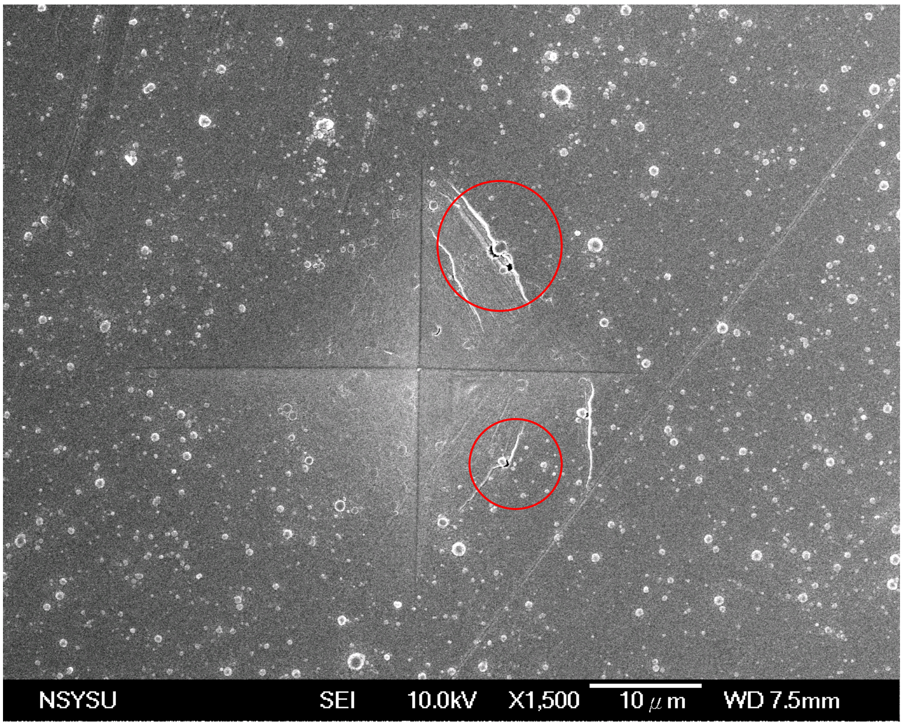

Figure 4-17 The SEI image of the $Pd_{77}Cu_6Si_{17}$ TFMG 1000 nm in thickness at an applied load of 50 g.

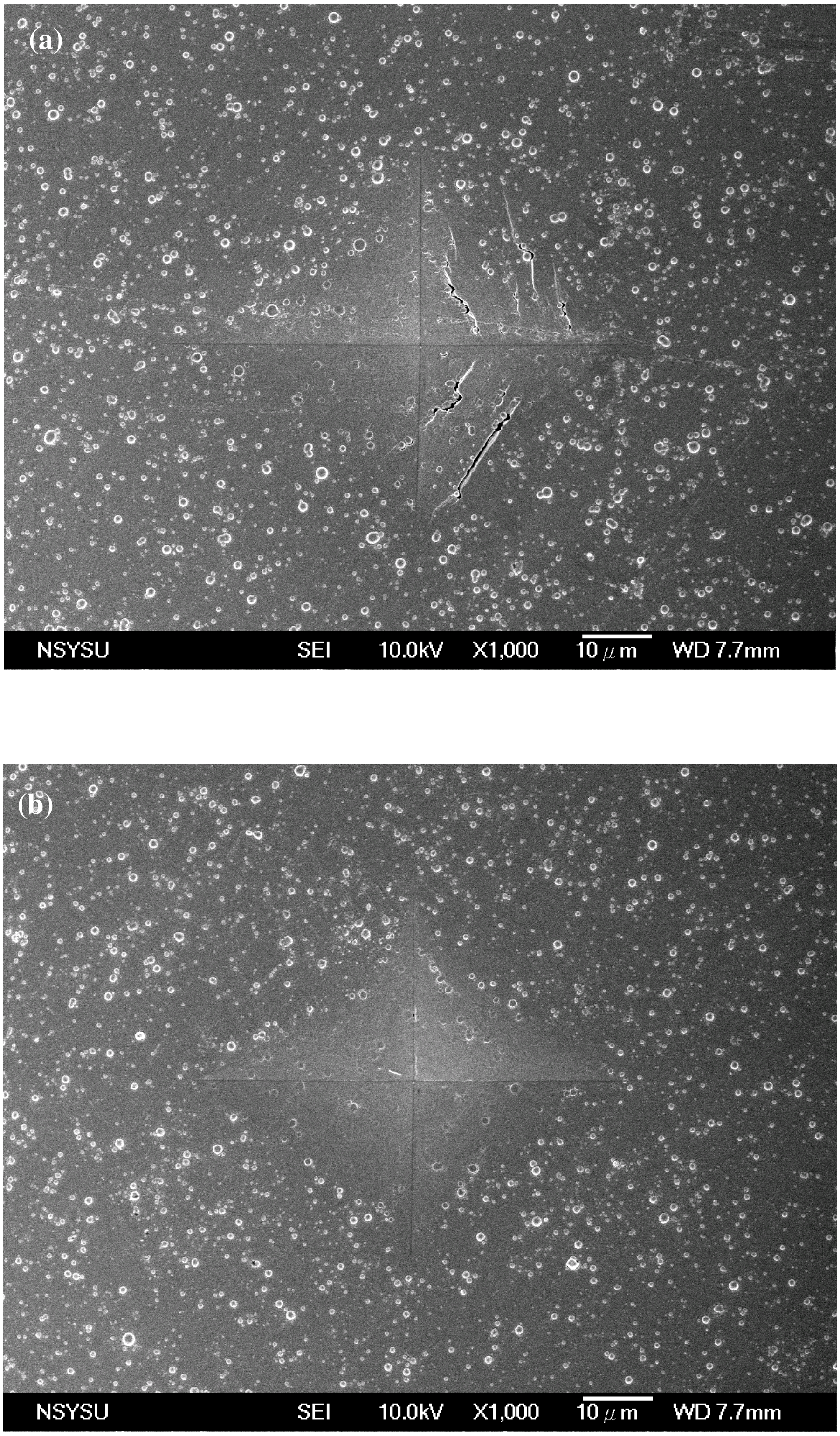

Figure 4-18 The SEI image of the $Pd_{77}Cu_6Si_{17}$ TFMG 1000 nm in thickness (a) with obvious cracks, and (b) without any crack at an applied load of 100 g.

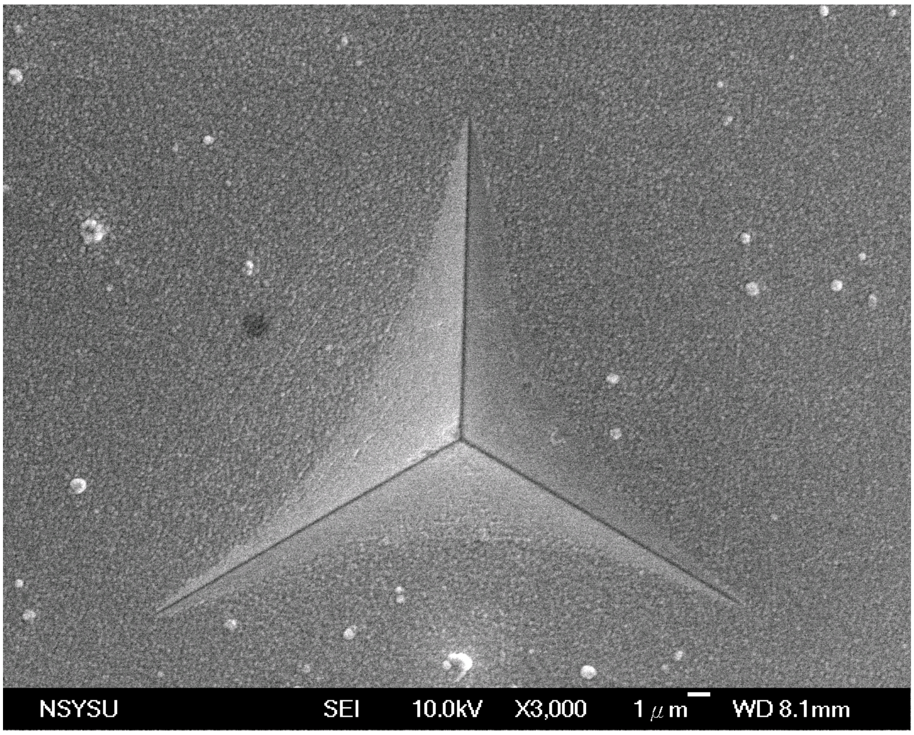

Figure 4-19 The SEI image of the $Pd_{77}Cu_6Si_{17}$ TFMG 2000 nm in thickness under nanoindentation testing.

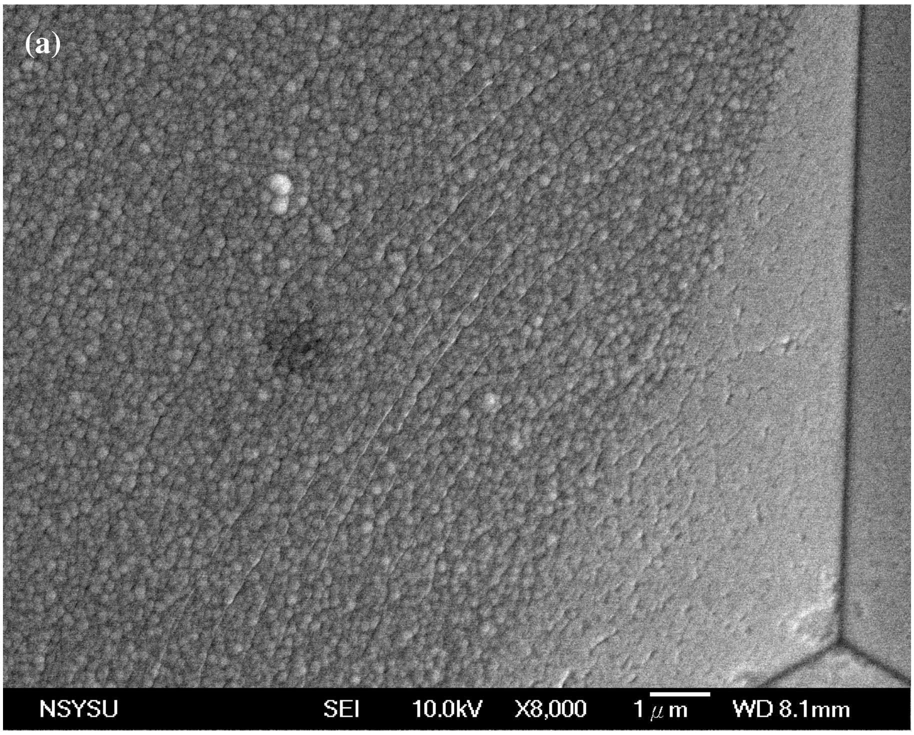

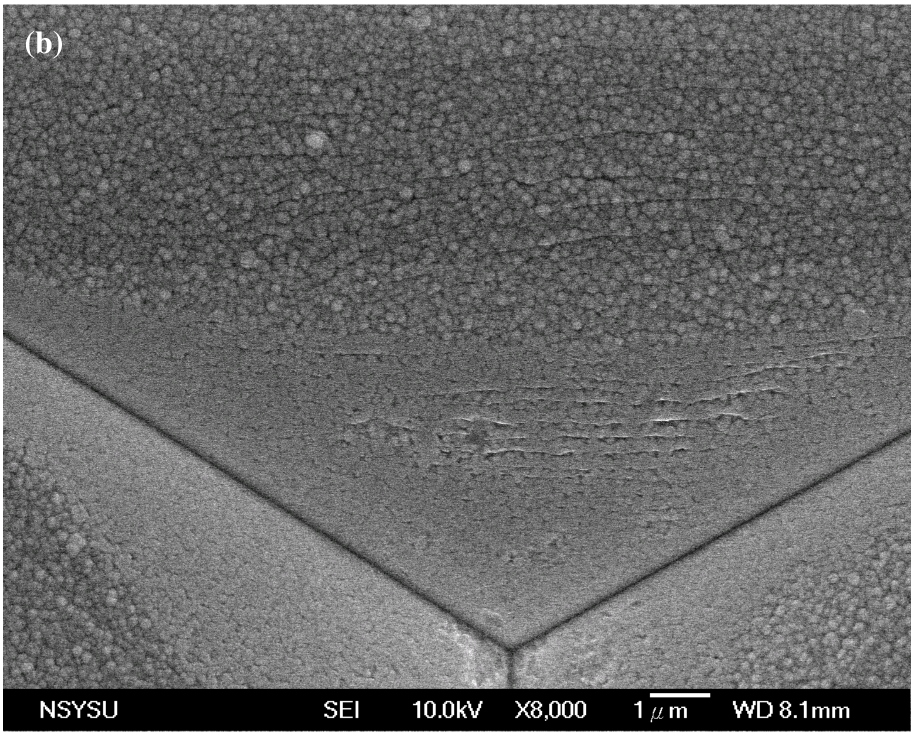

Figure 4-20 (a) The enlarged SEI image (b) the enlarged and rotated SEI image of the $Pd_{77}Cu_6Si_{17}$ TFMG 2000 nm in thickness under nanoindentation testing.

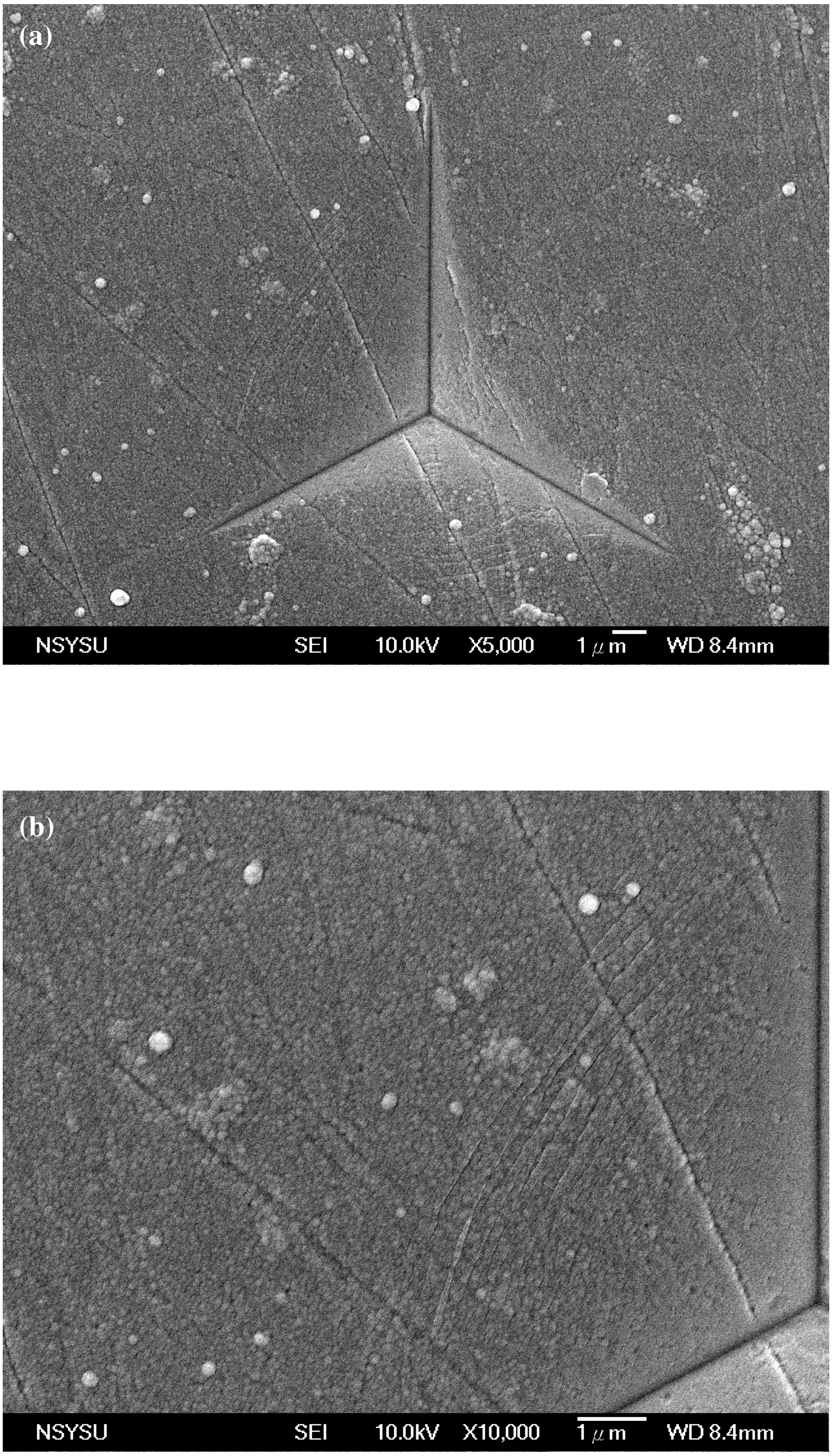

Figure 4-21 (a) The SEI image of the $Pd_{77}Cu_6Si_{17}$ TFMG 1000 nm in thickness under nanoindentation testing. (b) the enlarged SEI image taken from Figure 4-23 (a).

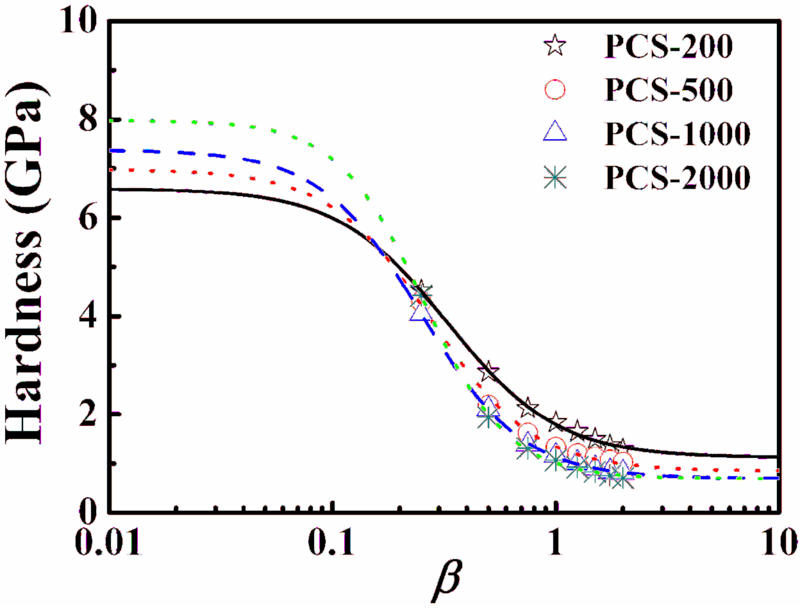

Figure 4-22 Comparison of the experimental data (in various symbols) and the best fit predictions based on equation 4-3 (in various lines) for the PCS 200, 500, 1000 and 2000 samples under nanoindentaiton. Note that the horizontal axis is presented in log scale.

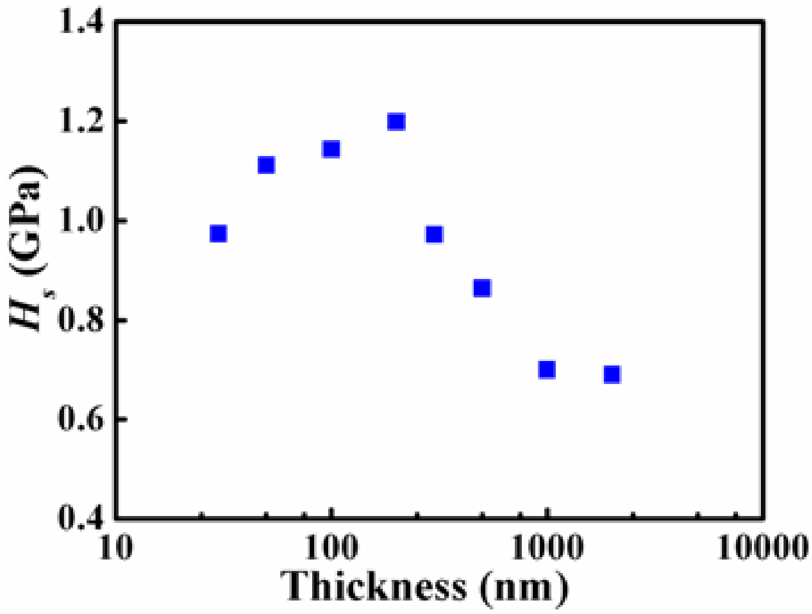

Figure 4-23 The predicted and postulated trend of the relative minimal substrate hardness H_s as a function of the surface hard coating thickness. The optimum hard coating thickness might be around 200 nm.